universität wien

MASTERARBEIT / MASTER'S THESIS

Titel der Masterarbeit / Title of the Master's Thesis

„Nucleosynthetic Yields of Population III Core-Collapse Supernovae“

verfasst von / submitted by

Martina Maria Koppitz, B.Sc.

angestrebter akademischer Grad / in partial fulfilment of the requirements for the degree of

Master of Science (MSc)

Wien, 2022 / Vienna, 2022

Studienkennzahl lt. Studienblatt / degree programme code as it appears on the student record sheet:	UA 066 861
Studienrichtung lt. Studienblatt / degree programme as it appears on the student record sheet:	Masterstudium Astronomie
Betreut von / Supervisor:	Univ.-Prof. Dipl.-Phys. Dr. Bodo Ziegler

Acknowledgements

I would like to express my deepest thanks to Daniel Whalen from the University of Portsmouth who guided me through the work and this thesis. No matter if challenges with the software or hardware came up, he always had an open ear and, if need be, redirecting me to a colleague. Under his supervision, I did not only get an insight into scientific research but also hands on experience in collaborating with experts from different countries.
I am extremely grateful to Bodo Ziegler for all his support and for agreeing on being my supervisor. Thank you for including me in your group, for the inspiring weekly group seminars and for giving me good advice when needed!
My sincere thanks go to Ken Chen from the Institute of Astronomy and Astrophysics in Taiwan. Without his support of providing his `CASTRO` setups and being always helpful when issues and questions arose, this work would not have been possible. Besides sharing his expertise with me, he regularly cheered me up by assuring me that the challenges I was facing are normal and that I am pushing through them the correct way.
Special thanks to Alexander Heger from Monash University for computing and providing the stellar progenitor models used to perform for the studies in this thesis.
I must also thank Jascha Schewtschenko for his patience and endurance in helping me at the very beginning with getting the `CASTRO` code running on `Sciama`!
I would also like to thank the `Sciama` support team, especially Toby Maule for installing necessary software on the machine and for always finding a solution for every issue I had in this context.
Many thanks to Anna Schrenk, my fellow sufferer, for supporting me in so many ways: keeping my spirit up during the pandemic to work on my thesis, offering help with the data analysis and giving me the feeling of not being alone with my thesis-related problems.
I would also like to express huge thanks to Konstantin Kirner for his proofreading and elephantastic support during all this time.
Finally, I would also like to thank the team of the IRRAD facilty at CERN with whom I have worked as a summer student this summer, namely Blerina Gkotse, Federico Ravotti and Giuseppe Pezzullo. Although not directly involved in this work, they provided me with an amazing environment and supervision that boostered my motivation.
Numerical computations were done on the Sciama High Performance Compute (HPC) cluster which is supported by the ICG, SEPNet and the University of Portsmouth. Analysis was carried out using `Python` programming language, including the packages `matplotlib`, `numpy` and `yt`.
Visualization of data was done using the `ViIt` visualization tool developed originally by the US Department of Energy's Advanced Simulation and Computing Initiative (ASCI)[1].

Abstract

Population III (PopIII) stars were the first stars that inhabited our universe. Through stellar nucleosynthesis they fuse nuclei heavier than hydrogen and helium. With their deaths, these elements are ejected into the interstellar medium. Their importance as the primary enrichers of the cosmos is undisputable and crucial for the cosmic chemical evolution, yet their properties still remain fragmentary. Due to their high redshifts at z $10 - 20$ and weak brightnesses, direct observations with today's and the next generation of observatories are impossible.
Nevertheless, there are ways to obtain information by searching for their descendants, the successive generation of stars, called PopulationII (PopII). Formed from the ashes of the previous generation, they carry an imprint of their elemental composition. Analyzing their abundance pattern can reveal not only the properties of the first stars but also give insights into their deaths. Simulating their ends, computing their ejected material and matching these results to observed abundances is how stellar archaeology proceeds to unravel the mysteries of the first stars.

The present thesis will investigate the nucleosynthetic yields of two PopIII core-collapse supernovae 12.4 $M_\odot$ with explosion energies of 0.3 B and 0.9 B. Hydrodynamical simulations are performed to model evolution and expansion of the process. Special emphasis is taken to study mixing of the shells inside the stars during shock propagation as well as fallback onto the compact remnant which determine the nucleosynthetic yields in the end, particularly for heavier metals.
Stellar progenitor models were already evolved in a stellar evolution code, all the way from the start of central hydrogen burning on the main sequence until the onset of collapse of their iron cores. This object now carries all the information about the elemental abundances created inside the star through stellar nucleosynthesis during its life and its arrangement in shells around the iron core. An explosion is triggered by the deposition of linear momentum at energies of 0.3 and 0.9 Bethe (1Bethe = 10^{51} erg = 10^{44} joule). These 1D models are mapped on the 2D `CASTRO` grid using a conservative mapping scheme to ensure conservation of mass and energy.
The goals of my thesis are modelling fallback and mixing and deduce the chemical yields of the elements ejected by the supernova. Discuss differences between the run two models, and the results presented in the paper of Chen et al. [2]. Furthermore, results of the two explosion energies are compared to the chemical composition of one of the most iron-poor stars known so far, namely J031300.
Knowing such detailed Pop III supernovae nucleosynthetic yields not only helps us constrain properties of the first stars, but also to constrain at what time the first habitable worlds in our universe may have formed.

Kurzfassung

Die ersten Sterne, Population III Sterne genannt, spielen eine bedeutende Rolle in der chemischen Entwicklung des Universums. In dessen frühen Phasen bestand es fast ausschließlich aus Wasserstoff und Helium, da Energien während der primordialen Nukleosynthese nicht ausreichten um schwerere Kerne zu bilden. Erst durch stellare Nukleosynthese im Inneren der ersten Sterne wurden mit der Zeit schwerere Atomkerne gebildet. Durch ihren Tod schließlich wurde das All mit diesen Metallen angreichert, im astronomischen Kontext zu verstehen als jene Elemente schwerer als Wassertoff und Helium. Trotz ihrer großen Bedeutung bleiben die Eigenschaften der PopIII weiterhin unvollständig. Simulationen weisen darauf hin, dass ihre Massen im Allgemeinen höher sind als die der heutigen Sternenpopulation. Aufgrund ihrer hohen Rotverschiebung sind sie weder mit aktuellen, noch der zukünftigen Generation von Teleskopen direkt zu beobachten.

Dennoch gibt es Möglichkeiten ihre Eigenschaften näher zu untersuchen, indem die unmittelbar nachfolgende Sternengeneration studiert wird. Genauer gesagt werden extrem metallarme Sterne beobachtet und deren Zusammensetzung erforscht. Unter Annahme, dass diese Population II Sterne durch die Überreste eines bzw. sehr weniger PopIII Sterne angereichert wurden, können ihre Isotopenhäufigkeiten mit denen aus theoretischen Vorhersagen verglichen werden. Je nach Eigenschaften der Sternen, allen voran der Masse, werden unterschiedliche Elemente in der Nukleosynthese generiert. Abhängig von der Art und genauerem Mechanismus des Sternentodes ergibt sich eine bestimmte Menge an Isotopen, welche schließlich in das interstellare Medium ausgestoßen werden. Dieses modellierten Häufigkeiten lassen sich anschließend mit denen aus Beobachtungen von extrem metallarmen Sternen abgleichen. Somit lassen sich Übereinstimmungen finden, welche wiederum Rückschlüsse auf die Eigenschaften der ersten Sterne zulassen.

In der vorliegenden Arbeit werden die Kernkollaps-Supernovae zweier nichtrotierender PopIII Sterne mit 12.4 $M_{\odot}$, jedoch zwei unterschiedlichen Explosionsenergien mithilfe des `CASTRO` Codes simuliert. Die Sternmodelle wurden zunächst mit dem Sternentwicklungscode `KEPLER` bis hin zum Einsetzen des Kernkollaps entwickelt. Die Explosion selber wird über Hinzufügen von Impuls in Gang gesetzt und anschließend auf das 2-dimensionale Netz von `CASTRO` übertragen. Ziel ist es, mittels hydrodynamischer Simulationen das Vermischen und den Rückfall des Materials sowohl während der Supernova, als auch der folgenden Ausbreitung nachzustellen.
Des Weiteren werden die Resultate mit der chemischen Zusammensetzung eines der metallärmsten Sterne J031300 verglichen um nach Parallelitäten in den Isotopenhäufigkeiten zu suchen.

Contents

List of Tables

List of Figures

1 Introduction

The following chapter will give an introduction not only to the broader context of the thesis but also describe the motivation behind the studies performed in this work.
First, a brief description of the primordial universe is provided. Next, after discussing the formation process of the very first stars in this environment, their possible deaths depending on the mass are explained. The mechanism of core-collapse supernovae is talked about in more detail, followed by a discussion about the observational contraints of these events.
Finally, the concept behind stellar archaeology is described and practically illustrated for the case of J031300, one of the most metal poor stars observed up to date.

1.1 The Early Universe

Edwin Hubble's milestone discovery in the 1920s about the expansion of the universe set the premise for todays' understanding of the history of our cosmos as illustrated in figure 1.1. Going back in time, space must have been denser, hotter and smaller. The universe is considered to have started with the Big Bang 13,8 billion years ago. After a few seconds, the universe cooled down enough so that quarks could start forming protons and neutrons.
Subsequently the first nuclei started forming in the following period of primordial nucleosynthesis. After 20 minutes, hydrogen and helium and trace amount of lithium and beryllium have formed. Heavier nuclei could not form due to insufficient temperatures

and the lack of stable nuclei with mass numbers of 5 and 8. Temperature and density continued to decrease as the universe, filled with a mixture of free moving nuclei, electrons and photons continued to expand.

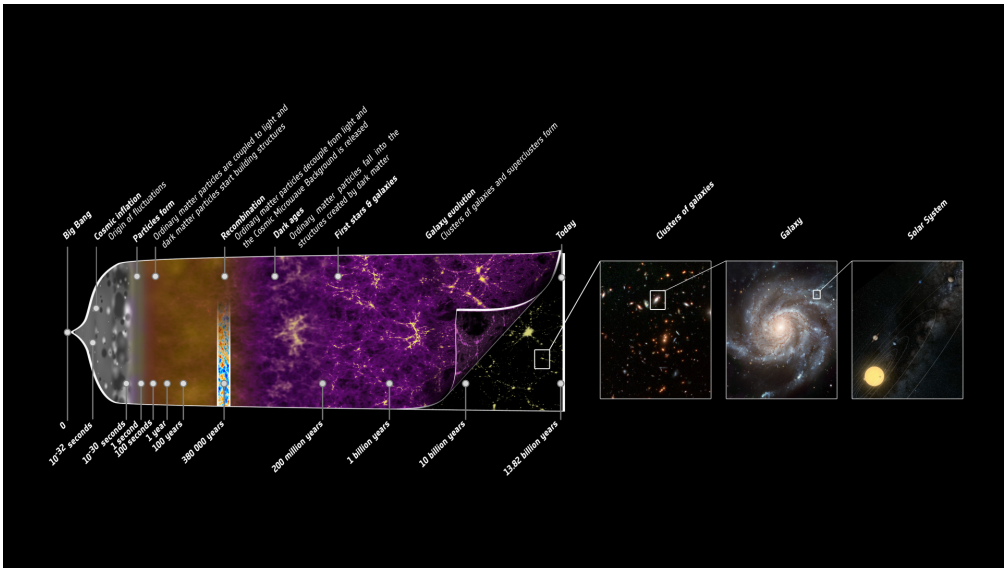

Figure 1.1: Overview over some milestones in the history of our universe. Formation of the first stars 200 Myr after the Big Bang ended the dark ages and marked the beginning of the reionization epoch.[3]

After 380000 years, the universe cooled down to temperatures around 3000 K, enabling the electrons and nuclei to combine into neutral atoms. During this epoch, radiation and matter decoupled from each other and resulted in the photons being now able to travel freely through space without being scattered. The afterglow of this recombination can still be observed as the cosmic microwave background. It also shows the tiny density fluctuations in the primordial matter distribution which are considered the seeds for the development of the first structures in our universe. Dark matter as well as baryonic matter started to gather in these locations. The following dark ages were finally after 200-300 Million years with the formation of the first stars inside these minihalos.

1.2 Primordial Star Formation

Stars are observed to form inside cold clouds consisting of gas and dust. These object range in terms of properties up to 200 lightyears in diameter and temperatures down to a few Kelvin. Inside, protostellar cores and eventually stars can form when the gravity of the gas gets higher than the stabilising pressure caused by the motion of the particles. The gravity acting between the molecules in the cloud and trying to compress the structure. On the other hand the kinetic energies of the molecules which generate a pressure acting against the gravity and keeping the cloud stable. Properties like temperature, density, mass and magnetic fields have an impact on the stability and either enhance or suppress the star formation. The so called Jeans mass describes the required mass for a spherical gas cloud to collapse under its own gravity:

$$M_J = \left(\frac{5kT}{G\mu m_H}\right)^{\frac{3}{2}} \left(\frac{3}{4\pi\rho}\right)^{\frac{1}{2}} \tag{1.1}$$

with ρ being the density, k the Boltzmann constant, T the temperature, μ the molecular weight and G the gravitational constant [4].

The very first stars, however, differed in their formation process from the other two populations. Describing the star formation in the early universe, we are facing several major dissimilarities in the composition and arrangement of matter compared to its state today.

To properly understand star formation in the early universe the initial conditions have to be taken in to account. Thermodynamical behaviour of the gas, meaning their heating and cooling mechanisms will determine the capability of the system to collapse and form stars. With only hydrogen and helium present the understanding of their atomic and molecular physics is crucial. Furthermore, the evolution and formation history of dark matter halos needs to be included. Computing the formation process with regard to all these contributions is possible via simulations with supercomputers.

The first stars are considered started forming at redshifts of z $20 - 30$ inside of dark matter minihaloes of masses $10^5 - 10^6$ $M_\odot$ [5]. For long time it was thought they formed solitary and reached high masses [6]. More recent simulations assume that PopIII stars can either form alone, in binaries or small groups.

DM minihaloes form as a result of the density perturbations in the early universe which started collapsing. Through filamentary inflows, the baryonic gas starts to accumulate in these regions. Together with the dark matter component, this virial system can be described through the potential and kinetic energy:

$$\frac{GM_h}{R_{vir}} \sim v_{vir}^2 \tag{1.2}$$

with M_h being the total mass of the halo, v_{vir}^2 and R_{vir} the virial velocity and radius [7]. As a consequence of the collapse and virialization process the gas will heat up. This virialization temperature can be further described by adding the virial velocity of the DM particles to above equation [6]:

$$T_{vir} \backsimeq 2 \cdot 10^3 K \left(\frac{M_h}{10^6 \mathrm{M}_\odot}\right)^{\frac{2}{3}} \left(\frac{1+z}{20}\right) \tag{1.3}$$

Typical values for the gas temperature lie around 10^4 K. Further cooling below this temperature can only be achieved by molecular instead of atomic hydrogen. However, formation of molecular hydrogen probes to be complex. Without the presence of dust grains to absorb the excess of energy abundant through the bonding of the two hydrogen atoms, different pathways must be taken into account. By reacting with itself and free electrons, the three main pathways are [8]:

$$H + e^- \rightarrow H^- \text{ then } H^- + H \rightarrow H_2 + e^-$$

$$H^+ + H \rightarrow H_2^+ \text{ then } H_2^+ - + H \rightarrow H_2 + H^+$$

$$H + H + H \rightarrow H_2 + H$$

The first two dominate at densities $\lesssim 10^8 cm^{-3}$, the last one above this value.

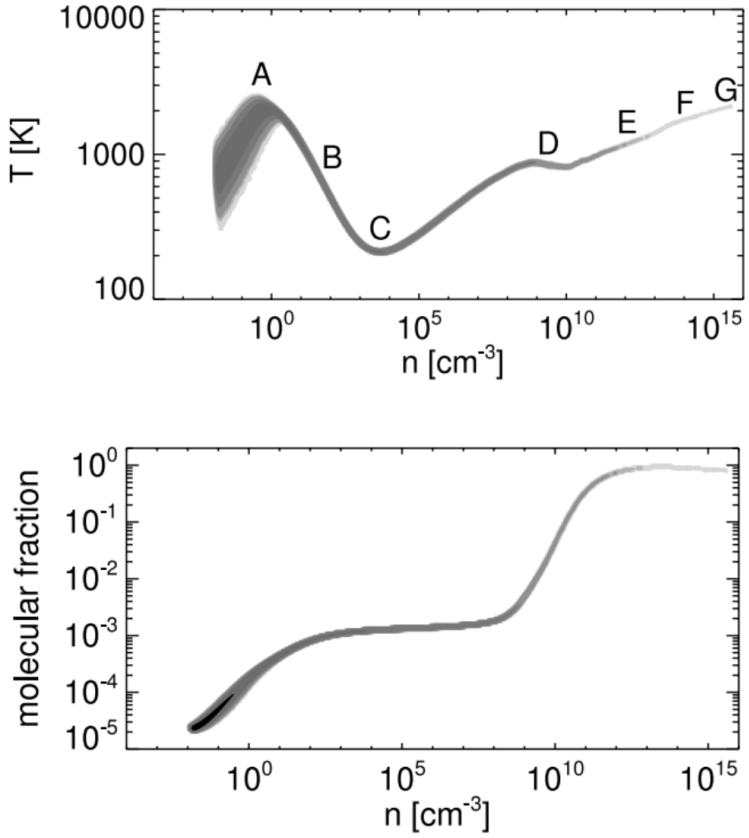

Figure 1.2: Overview over density and temperature evolution in a spherical collapse system. (A) via virialization process, gas reaches temperatures about 10^4K, (B) cooling via molecular hydrogen down to temperatures around 200 K, (C) saturation of H_2 cooling rate (D) transition to fully molecular gas via three-body formation pathway (E) as opacity increases, cooling rate decreases (F) cooling through collisions becomes dominant (G) H_2 dissociation at temperatures 200K [9]

H_2 will build up asymptotically during the first phases of the collapse through rovibrational transitions. For higher densities, full conversion into H_2 via the three-body reactions is reached which results in a run-away cooling phase. In very massive and externally irradiated halos, even cooling via hydrogen deuteride can enter the picture. Through this process, even gas temperatures below 200 K can be reached. At this point of the collapse, a protostellar core will have formed in the center of the halo which can further grow via accretion and infall of surrounding material and the gas heats up again. With the three-body H_2 formation setting in, the gas becomes fully molecular.
When densities reach the regime of around $\rho > 10^{14} cm^{-3}$ and molecular lines become optically thick so that cooling will be further enhanced via $H_2 - H_2$ configuration.

1.3 Final Fate of Population III Stars

With the simulations hinting towards the fact that Population III stars could have been more massive than stars in todays' universe, more pathways for the final fates at the end of their lifetimes have to be considered. The most crucial parameter regarding their evolution and death is mass. Due to their composition of pristine gas, mass losses throughout their lifetime are strongly reduced compared to stars of the two other generations [10]. Consequently, they keep their initial masses all the way through the process of central helium burning. As a result, when discussing PopIII deaths, their final fates can be directly linked with their initial masses.
Stars are held together by their gravity which additionally compresses the star. Temperatures and densities reach immense dimensions in the stellar core, thus enabling nuclear fusion to take place. This thermonuclear reactions produce an outward directed pressure which acts against gravity and ensures the hydrostatic stability of the system.
During the first stage of nuclear fusion, hydrogen is being fused into helium, requiring temperatures above $\sim 10^7$ K. This reaction is realized mainly via three proton-proton

chains. The helium core is not formed directly from four hydrogen nuclei but instead through intermediate steps via formation of deuterium and tritium. In stars with sufficiently high temperatures in the core as well as carbon, nitrogen and oxygen abundant, another helium forming process called CNO-cycle can take place. After the exhaustion of hydrogen in the star's center, hydrogen burning is relocated to a shell around the core. When conditions in the core become suitable enough, meaning temperatures above 10^8K, helium fusion can set in. Two helium nuclei first form an unstable beryllium nucleus. If an additional alpha particle happens to be in the right time and place, they fuse and form a ^{12}C nucleus. Via this triple-alpha process, helium fuses to carbon and, provided the presence of essential conditions, even further to oxygen. Low and intermediate mass stars start leaving the stage after this point. Their masses are not high enough to ignite the next stages of stellar nucleosynthesis. They undergo a series of pulsations resulting in ejection of their outer layers, leaving behind a planetary nebulae and white dwarf, mainly composed of carbon and oxygen, as remnants.

Usually the mass marking the transition between low/intermediate mass stars and massive stars is considered around $8M_\odot$.

For high mass stars the nucleosynthesis is far from over: further fusion processes via carbon, oxygen, neon and silicon are able to set in. The end is finally reached with iron build up in the core. As the iron nucleus has one of the highest binding energies per nucleon, energy generation via iron fusion is not possible. This means that the star is not able to obtain its stable state anymore. Consequently, the outward pressure ceases, gravity takes over and the stars begins to collapse. The outward material starts falling inwards with high velocities onto the stellar core. It experiences a heavy compression, strong enough to force electrons to combine with protons in the atomic nuclei to form neutrons. This process releases a huge amount of neutrinos transporting away the energy of the process resulting in the reversion of the implosion and triggering an explosion.

These core-collapse supernovae (CCSN) are widely investigated today as the exact physics of their evolution still remains to be understood thoroughly. The remnant left behind after a CCSN is either a neutron star or, for masses higher than $20M_{\odot}$, a black hole . Figure 1.3 gives an overview over the outcome of a nonrotational PopIII star in dependence of their initial masses.

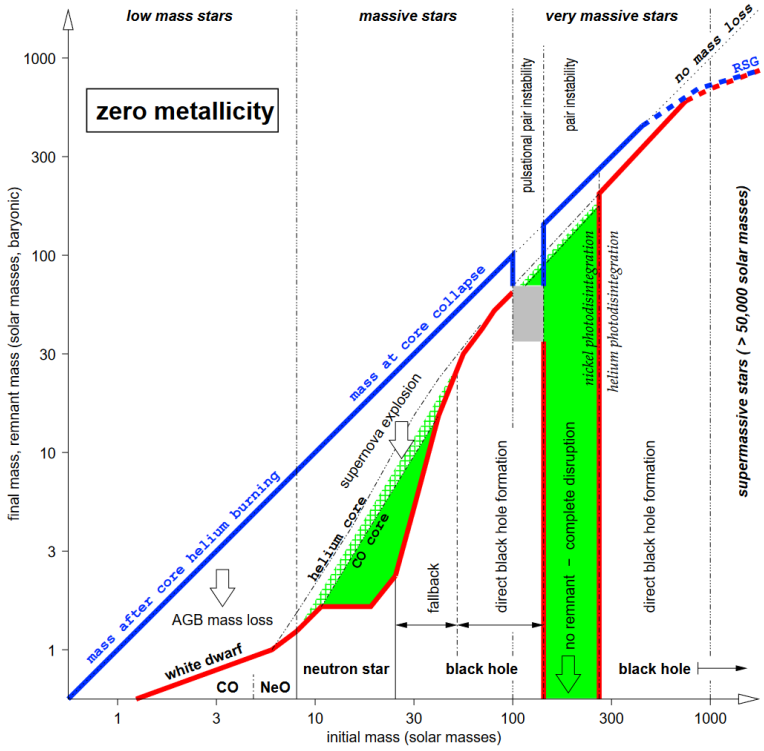

Figure 1.3: Possible fates of PopIII stars dependend on stellar mass. Shown are the masses at time of remnant formation/explosion (blue) and mass of the leftover remnant (red)

[10]

The mass limits must be considered as approximated values rather than fix values. Presence of metal abundances, rotation and mass loss may shift the limits to lower or higher values.

As numerical simulations predict the first stars inertial mass function being top-heavy, we

expect not only a higher amount of massive but also an significant population of very massive stars in the early universe. As the mass directly impacts the conditions inside the stars in terms of temperature, densities, convection etc., additional processes resulting from these extreme conditions need to be incorporated in the picture of final fates. In other words, the higher masses give rise to a broader spectrum of stellar dying processes. Stars in the mass range between $8M_{\odot}$ and $\sim 100M_{\odot}$ are labeled as massive stars, objects above that up to $1000M_{\odot}$ referred to as very massive stars and even beyond as supermassive stars.

Going more into detail, star inhabiting the mass range between $8M_{\odot}$ and $30M_{\odot}$ are considered to die as core-collapse supernovae leaving behind a neutron star as remnant. In the $30M_{\odot}$ and $90M_{\odot}$ mass range a black hole will form: for the lower masses via fallback, when material falls back an a previously formed neutron star causing further collapse of the object to a black hole. For more massive ones, the outward shock of the supernovae is not strong enough to expel the material and a direct collapse to a black hole will occur.

Stars with masses between $100M_{\odot}$ and $260M_{\odot}$ will die as pair instability supernovae. At the end of their lives, temperatures within the core climb high enough to produce positron-electron pairs from thermal photons. This process reduces the amount of thermal pressure stabilizing the core against gravity resulting in a contraction of the core. As a direct consequence, temperature rises which triggers a runaway thermonuclear reaction through ignition in the oxygen and silicon layers. In the lower mass range, the generated pressure loss and subsequent energy generation through this mechanism are not high enough to repel the overlying shells and destroy the star. Instead, they undergo several pulsational phases where the star is reaching its equilibrium again after a core contraction sequence. The concomitant mass loss of these pulsational pair instability supernovae causes the mass to drop to the regime where burning to an iron core and direct black hole collapse can occur. For stars above $140M_{\odot}$, the released energy ranging

up to 10-100 times than those of core-collapse supernovae, resulting in a complete disruption of the star without leaving a remnant.
Stars with masses higher than $260M_{\odot}$, even the extreme energy release by the thermonuclear runaway process is insufficient to halt the infalling material. As a result, direct formation of a black hole takes place, enhanced through photodisintegration instabilities.

1.3.1 Core-Collapse Supernovae

Contrary to the considerably well understood process in pair-instability supernovae, the explosion mechanism of core collapse supernovae still remains under investigation. The first approach in the early 1960s to formulate a theory where the core rebounds after contraction but further studies showed this mechanism fails to produce a robust supernova explosion. Instead, a neutrino driven explosion mechanism via the heating from neutrinos was first proposed in 1966 by Colgate and White [11].
At the end of its live, a massive star will have formed a degenerate iron core in its center, meaning that the degeneracy pressure of the electrons stabilises the core against gravity. As the core reaches its effective Chandrasekhar mass causing density and pressure to increase, photodisintegration of the iron nuclei into alpha particles and nucleons sets in. Additionally via the capture process

$$e^{-} + p \rightarrow n + v_e \tag{1.4}$$

the electrons are bound to protons in the nuclei releasing a tremendous amount of neutrons and leading to a destabilisation of the iron core. On the timescale of about one second, the core collapses and starts forming a neutron star. A shockwave is launched and eventually disrupts the star.

The shock increases the temperatures at its location within the first few seconds, triggering explosive nuclear burning and allowing nuclei ranging from carbon to zirconium to be formed.

While propagating towards the surface, the shock passes through the various elemental layers of the star, driving mixing.

Encountering shell with higher densities, a background shock forms triggering the development of Rayleigh-Taylor instabilities. More precisely, they form in spots where pressure and density gradient point in opposite direction. This feature arises during the shock propagation in the supernova. A reverse shock forms where it encounters a region of increasing ρr^3. This corresponds to shells of matter where the mass is larger compared to the previous one or, put another way, when a heavier fluid lies on top a lighter fluid [12]. Conditions notably found at the interface between elemental shells, especially between hydrogen and helium due to their properties. The back propagating reverse shock reverses the pressure gradient, thus pointing in the opposite direction of the density gradient. RT instabilities start developing and growing, mixing the material in the region and breaking the star's spherical symmetry.

Material with velocities too low to escape the gravitational pull from the remnant falls back to the center. The required escape velocity can be determined via [2]

$$v_{esc} = \sqrt{\frac{2GM_n}{r^2}} \tag{1.5}$$

with gravitational constant G, r being the radius and M_n as mass of the neutron star. This concerns both, material in the direct vicinity of the remnant and material pushed further inwards as a result of mixing.

These three processes, explosive nuclear burning, fallback and mixing determine the nucleosynthetic yields of a core-collapse supernova at the end. The postexplosional hydrodynamics have been investigated by numerous groups. To realistically model the

process of mixing, fallback and the linked Rayleigh-Taylor instabilities multidimensional simulations performed on supercomputers are required.

1.4 Observational Constraints

As mentioned above, the properties of Pop III stars are yet to be constrained as no direct observational evidence is available. Even with the next generation of infrared ground and space based observatories, the light of the first stars will most likely remain undetectable. Only effects like gravitational lensing could enable finding single stellar objects. Super massive Pop III stars as well as black holes, formed through their direct collapse, could be found by Euclid and the Nancy Grace Roman Survey Telescope at redshifts $z \gtrsim 10$ [13]. Designed for wide-field surveys covering up to several thousands of square degrees, they could be able to detect light which experienced gravitational lensing by massive galaxies and clusters. James Webb Space Telescope with its higher sensitivity could detect them at redshifts $z\ 10-20$, however its narrower field of view will make these kind of observations very challenging.

Another approach aims to search for signs of Pop III supernovae which release a significant amount of energy. Depending on their initial mass and explosion mechanism, the value and course of radiation release will vary. Production of radioactive isotopes and their subsequent ejection affect the output and leave an imprint in the light curves. Nickel 56 (half life 6.07 d) for instance which was formed inside the star via nuclear fusion decays to cobalt 56 (half life of 77.2 d)and iron 56 respectively will cause an observable rebrightening in the signal. Several investigations have been carried out to model the light curves of such supernovae [14]. Detecting these signatures with upcoming telescopes like James Webb Space Telescope, WFIRST and Euclid will not only allow to reveal PopIII

star masses but also information about their central engines and environments [14].

1.5 Stellar Archaeology

Another method to pinpoint the nature of Pop III stars is stellar archaeology.
In this indirect approach the abundance patterns of the most metal-poor stars, found in the galactic halo, are reconciled with theoretical nucleosynthetic yields of Pop III supernovae. The idea behind this procedure is that searching for stars with extremely low amount of metals in their composition eventually leads to finding stellar objects that were enriched by the very first generation of stars.

When Pop III stars end their lifes they eject part of their material. The composition of this material is determined by their mass as this parameter governs the course of stellar nucleosynthesis. Based on the following explosion mechanism, certain amounts of their previously fused elements are ejected and enrich the insterstellar medium. Pair instability supernovae per instance are supposed to provide yields imprinted with an odd even pattern [15].

In the standard notation for elemental abundances

$$[A/B] = log_{10}(N_A/N_B)_{star} - log_{10}(N_A/N_B)_{M_\odot} \tag{1.6}$$

N_A and N_B denoting the fractional abundances of elements A and B, the subscript $M_\odot$ describing the corresponding solar abundances [16]. Metal poor stars are often subdivided into several classes. Although this classification is not entirely uniform throughout the literature, [17] gives an overview over the most common adapted terms and limits in the field.

Metal-poor star related definitions

Description	Definition	Abbreviation[a]
Population III stars	Postulated first stars, formed from zero-metallicity gas	Pop III
Population II stars	Old (halo) stars formed from low-metallicity gas	Pop II
Population I stars	Young (disk) metal-rich stars	Pop I
Solar	[Fe/H] = 0.0	
Metal-poor	[Fe/H] < −1.0	MP
Very metal-poor	[Fe/H] < −2.0	VMP
Extremely metal-poor	[Fe/H] < −3.0	EMP
Ultra metal-poor	[Fe/H] < −4.0	UMP
Hyper metal-poor	[Fe/H] < −5.0	HMP
Carbon-rich stars	[C/Fe] > +0.7 for $\log(L/L_\odot) \leq 2.3$	CEMP
	[C/Fe] ≥ (+3.0 − $\log(L/L_\odot)$) for $\log(L/L_\odot) > 2.3$	CEMP
n-capture-rich stars	0.3 ≤ [Eu/Fe] ≤ +1.0 and [Ba/Eu] < 0	r-I
n-capture-rich stars	[Eu/Fe] > +1.0 and [Ba/Eu] < 0	r-II
n-capture-rich stars	[Ba/Fe] > +1.0 and [Ba/Eu] > +0.5	s
n-capture-rich stars	0.0 < [Ba/Eu] < +0.5	r/s
n-capture-normal stars	[Ba/Fe] < 0	no

Note – Carbon-rich stars appear with r- and s-process enhancements also. The CEMP definitions are from Aoki et al. (2007) and differ somewhat from Beers and Christlieb (2005)

Figure 1.4: Categories of metal poor stars listed in the literature, summarized by Frebel et al. [17].

1.6 Discussion of SMSS J031300-670839.3

One of the most-metal poor stars found up to date is SMSS J031300-670839.3 (hereafter referred to as J031300). Spotted by the SkyMapper Southern Sky Survey (SMSS) its age is being approximated to 13.6 billion years. The abundance pattern reveals an extremely low amount of metals, constraining that J031300 is indeed one of the first Pop II stars. Notably intriguing is the stars iron abundance which is less than one ten millionth compared to our sun and makes it the most iron poor star. The fact that almost no iron is evident in the spectrum of the star leads to the conclusion it was probably enriched with the ashes of one single Pop III supernova.

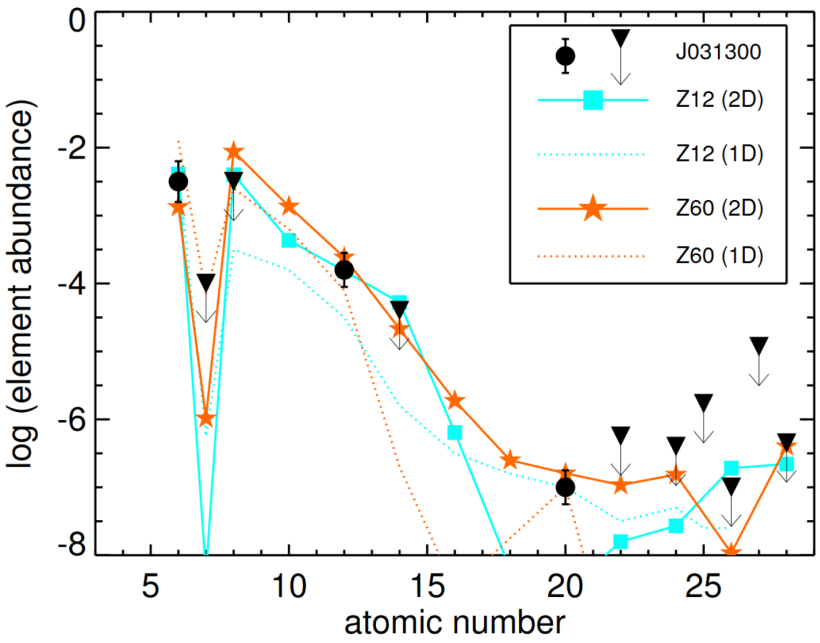

Figure 1.5: Abundance pattern of J031300 (black circles) compared to the modelled yields of the 12.4 $M_\odot$ and 60 $M_\odot$ progenitors. Results are displayed for both, those computed via the 2D `CASTRO` simulations and 1D `KEPLER` [2]

Based on comparisons between models and the abundance pattern of J031300, Keller et al. [16] proposed a 60 $M_\odot$ Pop III star as suitable progenitor. To account for the dwindling small amount of iron a low-energy supernova with an explosion energy of $1.8 \cdot 10^{51}$ erg was put forward. At such low explosion energies, the iron group elements in and near the center of the star do not reach high enough escape velocities to evade the gravitational pull from the compact remnant. Fallback sets in to pull the material back to the neutron star or black hole thus preventing it from being ejected and abundant in the yields.

Chen et al. [2] further pursued this approach and showed performing hydrodynamical simulations that even a 12.4 $M_\odot$ core collapse supernova could attend for the observed abundances. Figure 1.5 displays the measured abundance pattern of J031300 and compares it to the simulated yields of the 2D of the 12.4 $M_\odot$ and 60 $M_\odot$ star, as well as

for the expected 1D case. The authors come to the conclusion that the 60 $M_\odot$ star is a slightly better fit to the observed abundances than the 12.4 $M_\odot$ model confirming again that indeed the low iron group abundances can be explained through low explosion velocities. A linear momentum piston approach was applied for both models, with explosion energies of 0.6 for the 12.4 $M_\odot$ and 1.8 B 60 $M_\odot$ star. Both objects were first evolved in the stellar evolution code `KEPLER` until the onset of core collapse. Nucleosynthesis induced by the the explosion is followed until the temperatures drop low enough for the burning to end. The models are then mapped to the 2D grid of the `CASTRO` code where the subsequent evolution is tracked.

Comparison of both models is shown in figure 1.6. As expected, the shock breaks out way earlier of Z12 star as it is anticipated to end its life as a compact blue giant with smaller radius whereas the Z60 star becomes a puffy red supergiant. Taking a closer look at the formation and appearance of the fluid instabilities, they clearly arise earlier in the 12Z than in the Z60 model. The fingers of the Rayleigh-Taylor instabilities are also much finer than in the heavier star. After 44000 and 105000 s respectively, mixing is observed to be almost complete but fallback on the other hand still continues. With ceasing of the latter, the elemental yields are computed and compared to J031300.

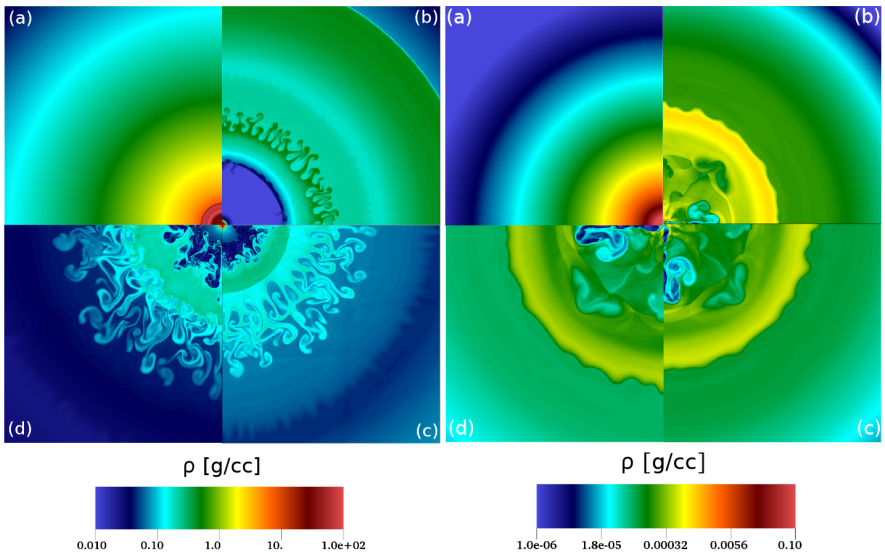

Figure 1.6: Densities inside the stars over the course of the explosion. For the 12.4 $M_\odot$ model on the left side the parcels correspond to (a)0s, (b)340s, (c)1200s, (d)2300s, in the 60 $M_\odot$ model on the right the evolution at (a)0s, (b)2100s, (c)9200s, (d)310000s is displayed.
[2]

2 Methods

The simulation of the supernova is performed in two stages. First, a progenitor star is evolved in the 1D KEPLER stellar evolution code [18]. Its evolution is tracked from the zero-age main sequence to the onset of core collapse. The explosion itself is realised by placement of a piston. This triggering via deposition of linear momentum with an energy of 0.6 Bethe (B) forms a shock at the base of the silicon burning shell. Bethe is a unit of energy equal to 10^{51} ergs = 10^{44} joule and used in supernova studies to express the released energy. The following nucleosynthesis via explosive burning is handled by KEPLER until 10 s after the collapse, when temperature drops below 10^9 K and nucleosynthesis is mostly completed. This state is now mapped onto the two dimensional CASTRO grid. To ensure conservation of mass and energy, the conservative mapping scheme described in [19] is applied. Mixing and fallback are modelled with CASTRO as the shock continues to expand.

2.1 Evolution of Progenitor Model in KEPLER

Modelling supernovae through all the stages of a stars life, from main sequence star until supernova and further process, in a multidimensional approach is still beyond the realm of present day computational capabilities. Therefore, the simulation procedure is performed in two steps. Initially, the progenitor star is evolved in one dimension with a stellar evolution code. The models used in this present thesis were generated with the 1D Lagrangian stellar evolution code KEPLER [18]. To target the main question about

studying differences in nucleosynthetic yields depending on altered explosion energies with regard to the discussed model in [2], a progenitor with 12.4 $M_\odot$ was chosen. The model was evolved from zero-age main sequence all the way through the stages of stable nuclear burning to the onset of core collapse. The explosion itself was triggered by deposition of linear momentum piston at the base of the oxygen shell [12] with energies of 0.3 and 0.9 B, respectively.

Subsequent steep rise in temperature triggers explosive nuclear burning processes being continuously recorded by `KEPLER`. Approximately ten seconds after the shock launch the temperatures drop to 10^9 K causing ongoing thermonuclear fusion processes to stop. At this point, the model carries all the information about the star in terms of nuclear species generated via fusion, location and strength of the propagating shock front inside the object. At this point, the profile is mapped onto the two-dimensional, cylindrical grid in `CASTRO`.

2.2 Mapping

The mapping of 1D model onto the 2D or 3D grid of hydro codes may induce numerical issues as well as challenges arising from the differing mesh properties. These effects can ultimately lead to violating the conservation of energy and mass during the mapping process.

One way to deal with these problems is applying linear interpolation algorithms to initialize the multidimensional grids from the one dimensional profiles [19]. However, regions comprising critical features which therefore require higher resolution pose a risk if the new grid fails to resolve these properties.

It is even more important when handling mapping of profiles computed on Lagrangian grids, onto Eulerian meshes like performed for the simulations in this thesis. In fact, Lagrangian descriptions are commonly used for stellar evolution codes due to their advant-

ageous properties. Here, the motion of fluids, more precisely the fluid parcels, is followed by the observer in space and time [20]. The mesh is therefore not a rigid construction but instead is distorted constantly along with the evolution. For Eulerian approach on the other hand, the mesh is fixed. Fluid flow is observed as it is propagating through the single cells of the grid over time.

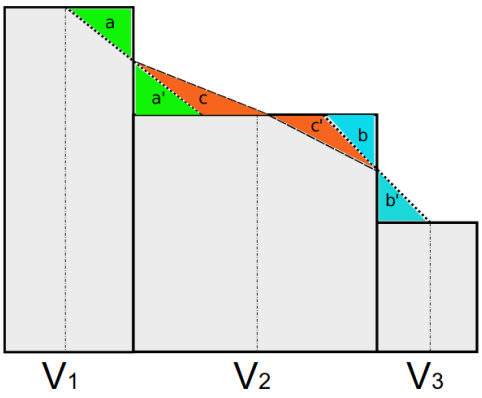

Figure 2.1: Bins represent the volume coordinates of the 1D profile, derived from the corresponding mass coordinate. Coloured areas on top illustrate conserved quantities obtained by piecewise linear reconsruction [19].

Figure 2.1 illustrates the mapping scheme. Goal is to conserve total energy while transferring the profile from the Lagrangian mass coordinate grid to the spatial Eulerian one. First step is to construct a function which preserves physical properties in the process. From the Lagrangian mass coordinate, corresponding volume coordinates are determined. Conserved quantities are obtained by integrating related densities with respect to these coordinate [19]. Next, an interpolation scheme is applied to determine the correct assignment of these quantities to the new grid. To summarize, the 1D profile's mass coordinates are assigned with new volume coordinates which are then utilized to determine the conserved quantities via a piecewise linear reconstruction method. Further details and validation tests of this scheme can be found in [19].

2.3 CASTRO

CASTRO is a multidimensional adaptive mesh refinement, radiation/MHD hydrodynamics code that is designed to model astrophysical reacting flows on massively parallel computers [21]. It uses an unsplit piecewise parabolic scheme and a general equation of state (EOS) to solve the equations of hydrodynamics. Besides of hydrodynamics and radiation it additionally includes the physics of full self-gravity and nuclear reaction networks and rotation. The code is build upon the AMReX C++ framework. This part of the code manages the adaptive mesh refinement (AMR), parallelization and memory management. The heavy computational procedures are done in Fortran kernels. The AMR comprises both space and time is realised via a nested grid hierarchy of logically rectangular grids [22].

The problems are solved on an Eulerian grid and support systems in spherical (one dimensional), cartesian (one, two and three dimensional) and cylindrical (one and two dimensional) coordinates. As the shock evolves over time and expands the shells of the star, enlarging the grid in order to capture all of the material necessary. This can be realised by restarting the simulation from any data output file. In the following runs the expansion of the star is followed until it reaches the boundary of the domain. The size of the grid is then doubled and the simulation can be directly continued from the last data output obtained on the smaller grid.

2.3.1 AMR

Adaptive mesh refinement (AMR) describes the method of adjusting the grid sizes locally when accuracy of the simulation requires a higher resolution. Not only does it help to save computational resources but simultaneously also allows to achieve high resolutions in turbulent regions. Wherever crucial physics happens on the mash, the AMR algorithm will mark those cells for refinement. They are hereupon divided in a recursive procedure

into finer grids.

To refine the mesh in regions of interest one has to specify the criteria for refinement. Thresholds for the values of upper and lower limits as well as gradients can be defined for quantities like pressure and densities. If these limits are exceeded during the execution of the simulation, the corresponding cells become tagged for refinement by `CASTRO's` built-in routines.

In the following runs, this process was allowed for up to 8 levels of refinement and a refinement ration of 2, resulting in a effective increase in resolution of 256. Combined with the root grid resolution of 256 x 256 it produces a simulation domain of 65536 x 65536 zones. In terms of computational resources, the simulations in this thesis were performed on 256 cores with 3.2 GB or 4 GB, depending on the chosen queue. Additionally, the computation process was further parallelized by enabling the MPI option in the `CASTRO` code.

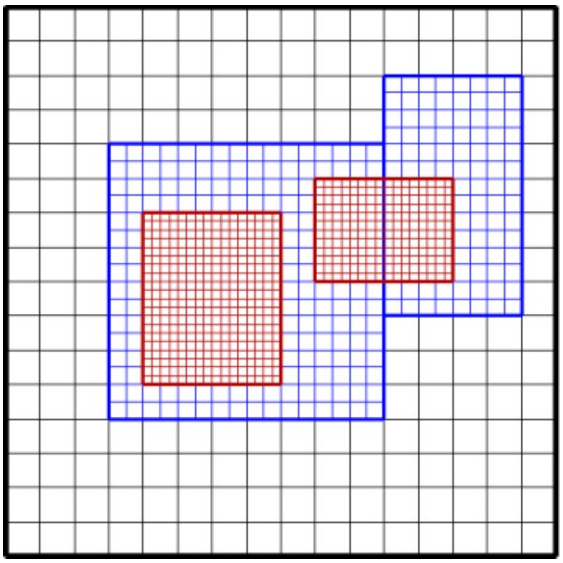

Figure 2.2: Scheme of AMR grids with refinement level of 2 and refinement ratio of 2 [22]

The number of repetitions depends on the parameters set by the user, as well as the number of refinement levels and the refinement ratio.

In terms of boundary conditions (BC), CASTRO offers six different types that can be set for the low and high directions of every coordinate. For the simulations in this thesis, reflective boundary conditions on the lower and outflow on the higher direction of the r and z grid are imposed. They govern the behaviour of the modelled fluid at the boundaries of the grid. The no-slip wall BC correspond to the concept of a solid wall, the free-slip wall a wall without viscous effect. Periodic boundary conditions can be applied when repetitive patterns appear in the problem. In- and outflow conditions are applied to problems where the flow either flows in or out at a specific location of a boundary. Due to the symmetry of the star, it allows us to only model one quarter of the problem and so reduce the size of the computational domain.

2.3.2 Physics

The following sections give an overview of the main physical components applied in the simulations. Although CASTRO comprises physics of radiation, magnetohydrodynamics and nuclear reaction networks, solely hydrodynamics and gravity are utilized in the present simulations as the motivation lies on studying impact of fallback an mixing. Therefore, these two components are described in detail.

Nuclear reaction networks are not incorporated in the present simulations as nuclear burning is considered to cease after $\sim 10s$ which is the time the 1D progenitor models are mapped onto the CASTRO grid. Nuclear burning reactions have already been fully modelled in KEPLER, therefore solely advection of isotopes is traced. Care must be taken regarding radioactive nuclei, in the context of supernova mainly ^{56}Ni. Particles emitted through their decay may reheat surrounding material, thus impacting dynamics. However, in the present models, the amount of ^{56}Ni is low enough to neglect this phenomenon. Species included in the runs are ^{1}H, ^{3}He, ^{4}He, ^{12}C, ^{14}N, ^{16}O, ^{20}Ne, ^{24}Mg, ^{28}Si, ^{32}S, ^{36}Ar, ^{40}Ca, ^{44}Ti, ^{48}Cr, ^{52}Fe, ^{54}Fe and ^{56}Ni. Listed species were particularly chosen in order to match the ones detected in JO31300, hence no more variation in isotopes in included.

Hydrodynamics

The physics of the studied system is governed by the fully compressible equations of hydrodynamics, also called Euler equations. As a set of partial differential equations derived from conservation laws, they describe the evolution of quantities characterising a fluid [23].

In `CASTRO`, they comprise the continuity equation expressing the conservation of mass 2.1, momentum equation 2.2, energy equation 2.3, advection equation 2.4, species equation 2.5 and an auxiliary term 2.6 as following:

$$\frac{\partial \rho}{\partial t} = -\nabla \cdot (\rho \boldsymbol{u}) + S_{\text{ext},\rho} \tag{2.1}$$

$$\frac{\partial (\rho \boldsymbol{u})}{\partial t} = -\nabla \cdot (\rho \boldsymbol{u}\boldsymbol{u}) - \nabla p + \rho \boldsymbol{g} + \boldsymbol{S}_{\text{ext},\rho \boldsymbol{u}} \tag{2.2}$$

$$\frac{\partial (\rho E)}{\partial t} = -\nabla \cdot (\rho \boldsymbol{u} E + p \boldsymbol{u}) + \rho \boldsymbol{u} \cdot \boldsymbol{g} - \sum_k \rho q_k \dot{\omega_k} + \nabla \cdot k_{th} \nabla T + S_{\text{ext},\rho E} \tag{2.3}$$

$$\frac{\partial (\rho A_k)}{\partial t} = -\nabla \cdot (\rho \boldsymbol{u} A_k) + S_{\text{ext},\rho A_k} \tag{2.4}$$

$$\frac{\partial (\rho X_k)}{\partial t} = -\nabla \cdot (\rho \boldsymbol{u} X_k) + \rho \dot{\omega_k} + S_{\text{ext},\rho X_k} \tag{2.5}$$

$$\frac{\partial (\rho Y_k)}{\partial t} = -\nabla \cdot (\rho \boldsymbol{u} Y_k) + S_{\text{ext},\rho Y_k} \tag{2.6}$$

where $\boldsymbol{u}$, T, ρ, k_{th}, p and E are the velocity, temperature, density, thermal conductivity, pressure and the total energy [22]. Furthermore, $\boldsymbol{g}$ denotes the gravitational vector, A_k an advected quantity and Y_k an auxiliary variable. Expressions denoted with upper case

"S "indicate source terms defined by the user. X_k represent mass fractions for species k with production rates $\dot{\omega_k}$ depending on the reaction network.
The equations are solved forward in time, using a second-order Godunov method and Riemann solver.

Equation of State

Solving the equations of hydrodynamics requires an adequate equation of state (EOS). It handles thermodynamic conditions of the fluid and therefore relates quantities of density, pressure and temperature and completes the problem description. Different physical properties of the gas and problem setup in general will affect the choice of the EOS. For instance modelling of low density interstellar medium will require different EOS than stellar matter. As latter scenario is the case for the simulations conducted in this thesis, the Helmholtz EOS as described in [24] was implemented. Including physics of both, degenerated and non-degenerated relativistic and non electrons, electron-positron pairs, radiation and ions, it provides a realistic description for stellar interiors [2].

Gravity

`CASTRO` provides three different approaches to incorporate self-gravity in calculations. In practice, the user needs to overall enable gravity in the settings, specifying type and corresponding parameters in the inputs file.
One possibility is to define a constant gravity field in terms of magnitude and direction. A more realistic method is provided with the monopole approximation approach. Here, the mass distribution is being integrated in spherical shells on the grid. This way, an enclosed mass is defined which is then used to compute the gravitational potential and the linked acceleration. For our model this means that a one dimensional density profile was created from the radial average of the density from the two dimensional grid. The resulting 1 dimensional gravitational potential is then applied in the run.

A more precise method utilizing a full Poisson solve is provided by `CASTRO` as well. It provides the option to calculate the gravitational potential by solving the full Poisson equation. For our problem setup, the monopole approximation is almost as accurate as the full Poisson approach with the benefit of being much faster [25].

2.3.3 Timestep Calculation

Solving the equations of hydrodynamics requires an adequate time stepping algorithm. Time step requirements chosen by the code are based on the Courant number. It is a dimensionless quantity linked to the Courant-Friedrichs-Lewy (CFL) condition which describes the requirements for stability of numerical schemes [26]. It describes the path length or the number of intervals that information propagates in a unit of time while moving through a computational grid:

$$C = \frac{U \cdot \Delta t}{\Delta x} \tag{2.7}$$

with Δt being the time step, Δx the interval, so practically the size of a mesh cell and U the flow velocity [26].
To ensure convergence of the calculation and therefore physically correct behaviour of the algorithm, the Courant number is set to a value between 0 and 1 as conventional for explicit methods, thus avoiding information to travel further than one cell during the applied time step.

In `CASTRO`, the calculations are performed on a fixed Eulerian mesh with the fluid moving through it.
Manual time step control is possible via setting a limit for the maximum value of level 0 timesteps as well as for the final simulation time [27].

Determination of the time step in all three dimensions is calculated via

$$\Delta t = \texttt{CFL} \cdot \min_{i,j,k} \left[\min \left\{ \frac{\Delta x}{|u|_{i,j,k} + c_{i,j,k}} \frac{\Delta y}{|v|_{i,j,k} + c_{i,j,k}}, \frac{\Delta z}{|w|_{i,j,k} + c_{i,j,k}} \right\} \right] \tag{2.8}$$

For 1D and 2D applications, v and/or w are neglected [27].

2.4 Software and Hardware

Simulations in 2D were performed with the `CASTRO` [1] code [21] as already stated in the beginning of the chapter.

Visualization was performed with `VisIt` [2]. It offers the option to visualize, animate and analyze data from both, vector and scalar fields defined 2D and 3D adaptive, structured and unstructured meshes [1]. Originally initiated and developed by the Department of Energy Advanced Simulation and Computing Initiative, it is now available as an open source tool and capable of handling over 120 scientific data formats.

Another tool utilized for quick visualizations of the outputted data sets was `amrvis` [3]. Designed for visualizing output from codes build upon the `amrex` [4] framework, it enables visualization of 2 and 3 dimensional data. Data analysis work was done using the `Python` package `yt` [5]. The community-developed, open source code is a toolkit for astrophysical visualization and analysis [28]. Developed specifically for the need of handling large data sets, it is able to deal with outputs of several simulation codes. Furthermore used `Python` packages include `numpy` [6] [29] and `matplotlib` [7] [30].

All simulations discussed in following thesis were performed using the resources of the

[1] https://amrex-astro.github.io/Castro/
[2] https://visit-dav.github.io/visit-website/index.html
[3] https://amrex-codes.github.io/amrex/docs_html/Visualization.html
[4] https://amrex-codes.github.io/amrex/
[5] http://yt-project.org
[6] https://numpy.org/
[7] https://matplotlib.org/

SCIAMA [8] High Performance Compute Cluster. Supported by the Institute of Cosmology and Gravitation (ICG), the University of Portsmouth (UK) and SEPNet it provides computational resources required for scientific research at ICG. The cluster comprises 4228 cores, 179 nodes, 1.8 PB Lustre storage, 4 A100 GPUs and specialised CPUs with 350 active nodes per board [31].

[8] http://www.sciama.icg.port.ac.uk/index.html

3 Simulations

In the following chapter, the performed simulations are discussed. First, data of the progenitor models are analysed. Velocity profiles of the material are studied as well as the location of specific elements shells. The quantity ρr^3 is displayed in order to pin down where instabilities will most likely begin to form.
Second, the evolution of fluid instabilities is examined by visualizing densities and species abundances at different times. Next, motions of the expanding material are discussed to study fallback. Finally, yields from the 1D progenitor model are determined and compared to the abundances of J031300.

3.1 Explosion Models

As the star was previously evolved in `KEPLER` to the onset of core collapse and then mapped onto the `CASTRO` grid, it is important to discuss the definition of time. After the explosion was triggered with a piston, the first seconds of the shock front evolution are still followed in the stellar evolution code to ensure capturing all the relevant explosive nucleosynthetic burning. 10 seconds after the shock launch, the model is mapped onto the `CASTRO` grid. On that account refer to this moment as t=0 and the following time specifications are associated with this start time. Checking the properties of the model at this starting time reveals the initial conditions at the begin of the `CASTRO` run. Figure 3.1 displays the one-dimensional velocities of the two explosion models dependent on the radius of the star. The step rise indicates the location of the shock inside the star.

As expected for a higher explosion energy, the shock front inside the 0.9 B model has travelled a further distance in ten seconds than in the 0.3 B one.

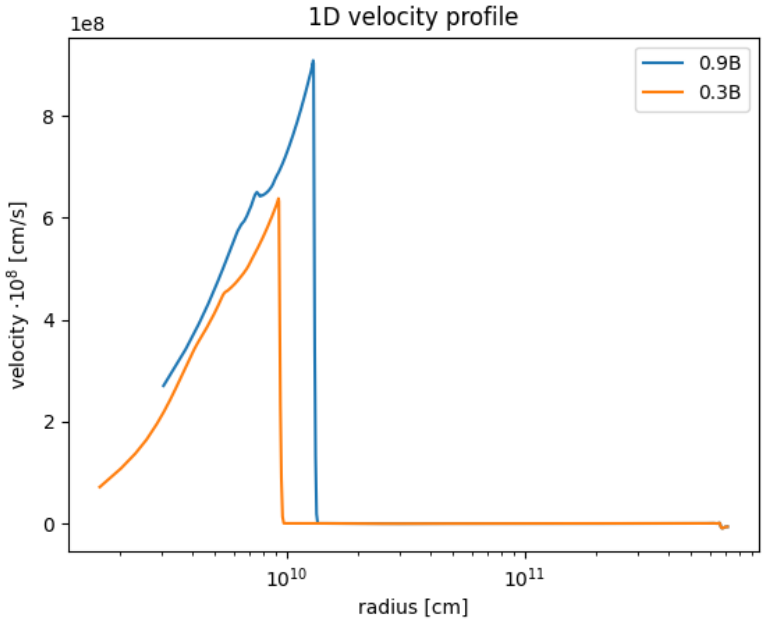

Figure 3.1: One-dimensional velocity profiles of the two explosion models at t=0, referring to the time when the star is mapped to CASTRO.

In comparison to the 0.6 B explosion discussed in figure 1 of [2], they are both still located in the more inner regions of the star as we are mapping the model to CASTRO after 10 seconds, while Chen. et al wait 20 seconds until mapping. In terms of peak velocity, we find a value of $6.4 \cdot 10^8 \frac{cm}{s}$ for the 0.3B model and $9 \cdot 10^8 \frac{cm}{s}$ for the 0.9B model. Depending on the remnant mass, escape velocities from the neutron star will vary. It can be determined via equation 1.5.

Calculations of nucleosynthetic yields with 1D models treat this value as a threshold determining a radius below which material in the vicinity of the center falls back onto the remnant.

3.1.1 Internal Structure

During its propagation outwards, the shock plows through regions with varying densities. Rayleigh-Taylor instabilities will likely form at such intersections of differing densities when certain conditions are met. The stars' internal structure, depending on the initial mass and metallicity of the star, will further determine the location and extent to which they grow. A strong indicator for their occurrence are regions in which the shock faces zones of increasing ρr^3.

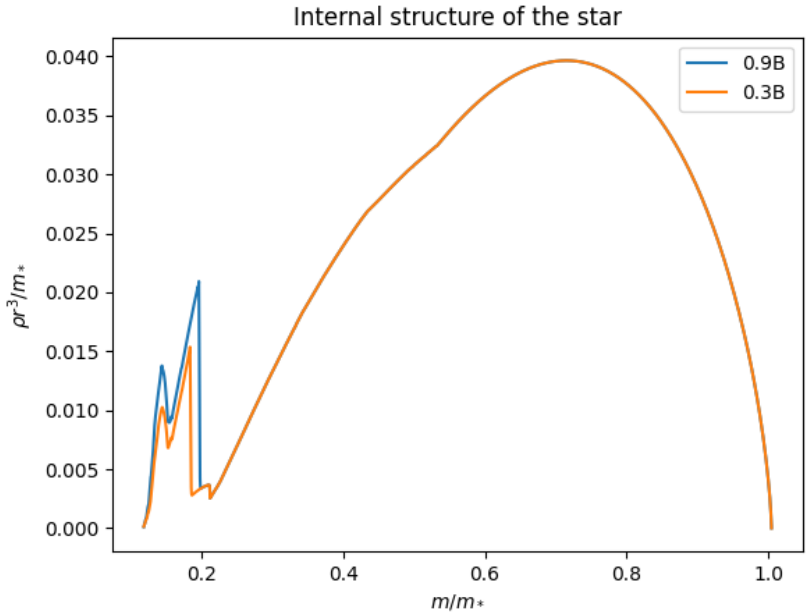

Figure 3.2: Internal structure of both explosion models at t=0. For the normalized mass in range of 0.2 to 1, only one line is visible as the of both coincides in this part of the star. Only closer towards the center, where shocks were launched with different explosion energies, a slight dissimilarity occurs.

Figure 3.2 displays the ρr^3 distribution normalized by the stars mass of both explosion models. Shown as a function of radius, the change of this quantity and especially increase will reveal regions inside the star that will give rise to the formation of a reverse shock. As the two models are of same mass and metallicity, their profiles show a high

similarity. In fact, the bulge between 0.2 and 1 m/m^* describing the envelope of the stars is exactly the same as no processes are abundant in the outer region yet to cause any dissimilarities. Closer to the core however, the development of ρr^3 in the two stars differs. It is lower for the 0.3 B explosion model compared to the 0.9 B one. The second peaks here close to 0.2 indicate the position of the shock, while the first one displays the detached reverse shock. Due to the higher explosion energy and the resulting compression of the material, ρr^3 is being shifted towards higher values.
The increase of ρr^3 at certain points is no coincidence but arises from the arrangement of the shells. To illustrate this fact, the distribution of both, hydrogen and helium in the two explosion models together with the ρr^3 course is shown in Figures 3.3 and 3.4.

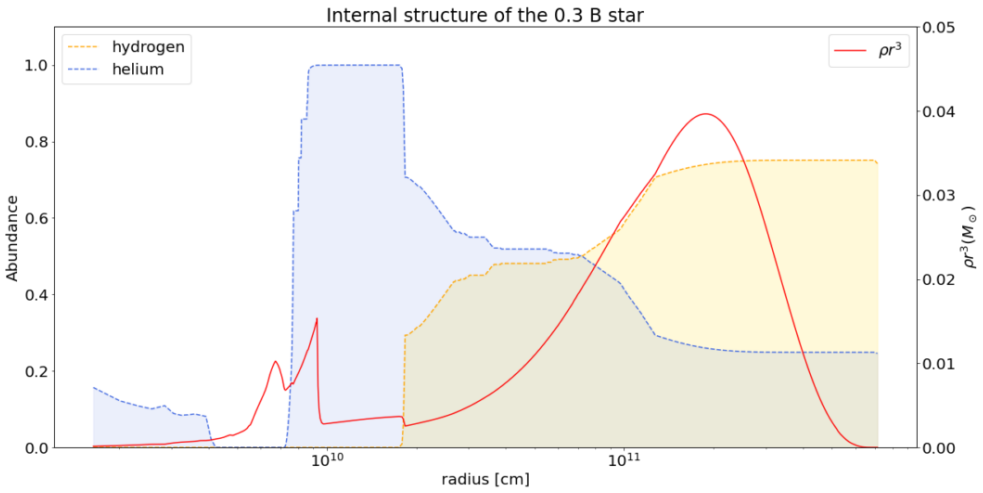

Figure 3.3: Internal structure of the 0.3 B explosion model at t=0.

The location of the hydrogen shell is again identical for both stars. For the helium shell however, the shape indicates some differences. The helium shell in the 0.3 B model reaches deeper towards the center. Helium abundances are also higher in the region closer to the center than for the 0.9 B star. Looking at the trend of ρr^3, its increase in the region around the location of the shock front marks the region where instabilities will

start forming. Overall, 0.9 B model shows stronger increase of ρr^3 which already indicates in this early stage of the supernovae that mixing will be most likely stronger in this model.

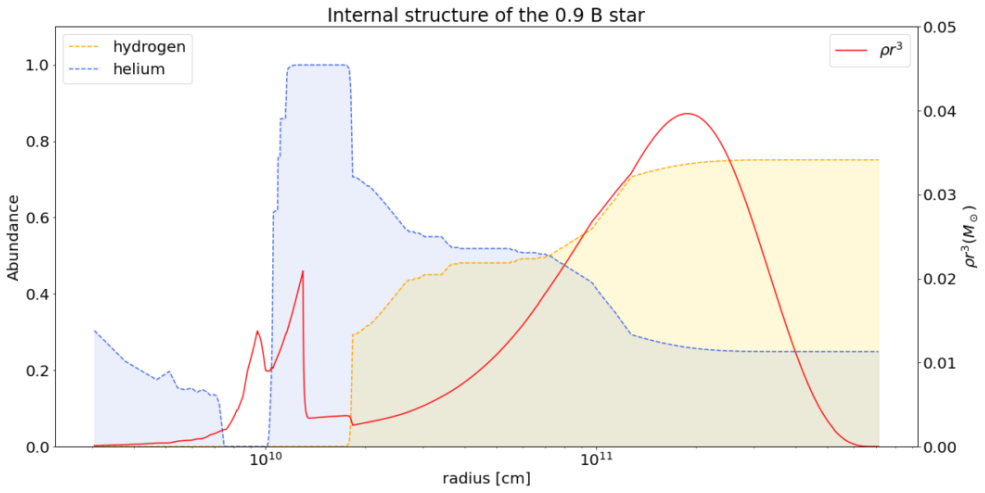

Figure 3.4: Internal structure of the 0.9 B explosion model at t=0.

The first steep rise of ρr^3 occurs at radii of around 10^{10} cm. More precisely, two distinct peaks are present in this zone. Analysing the structure and composition in this region reveals that the oxygen and carbon shells are located here. Their spread and exact position differs slightly between the two explosion models.

Both shells in the 0.3 B model can be found closer towards the center. Especially the oxygen shell is spread over a broader region. Figures 3.5 and 3.6 show that the shock has already passed the carbon and oxygen shell, due to the higher explosion energy it has already travelled further in the 0.9 B model. The first peak of ρr^3 is located at the inner boundary of the carbon shell, making it the region where the reverse shock is going to build up and therefore where the first RT instabilities will start to form. They first start growing exponentially during the reverse shock passing through, and afterwards linearly while the material is coming back to stability.

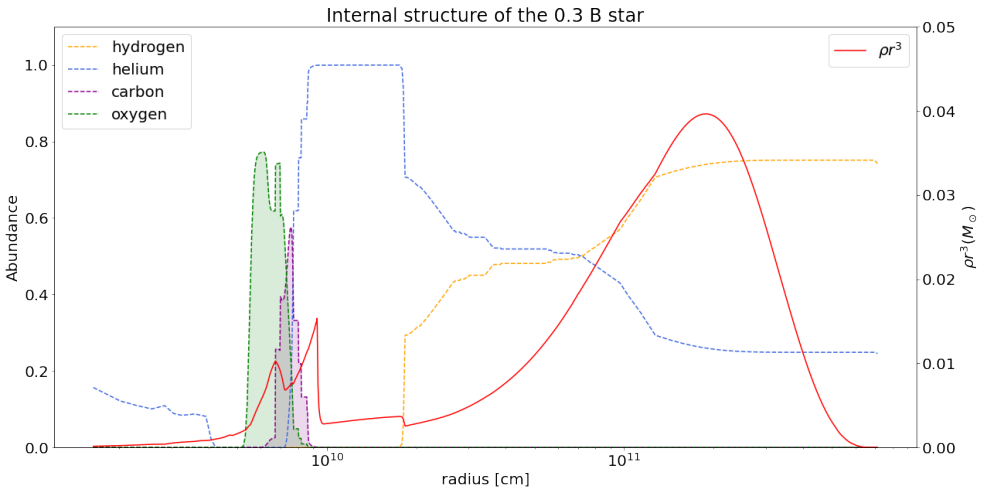

Figure 3.5: Internal arrangement of carbon and oxygen shells in the 0.3 B star at t=0. The shock, represented by the peak at 1010 *cm* passed both shells. Reverse shock, visible as the second, lower peak, already detached and will produce first RT instabilities at this intersection.

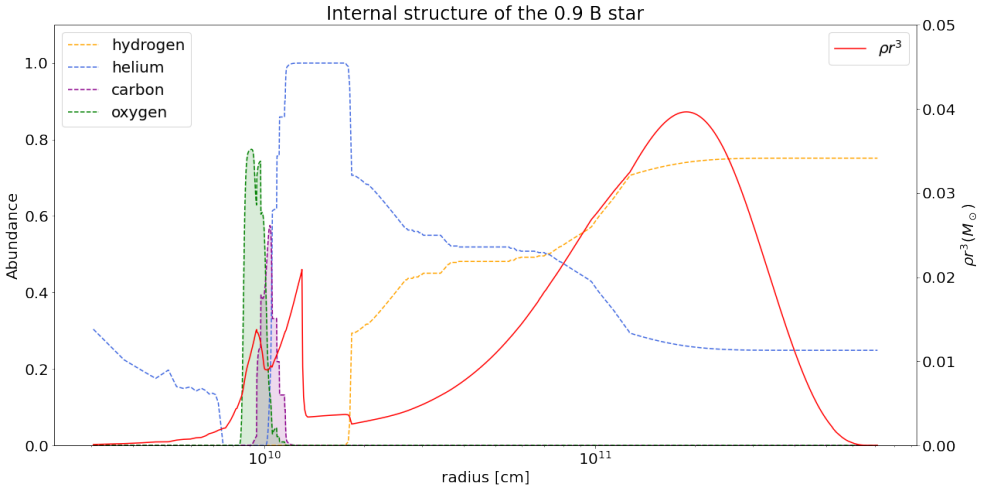

Figure 3.6: Internal structure of the 0.9 B explosion model at t=0. The stronger shock resulted in a higher rise of ρr^3 and larger travel distance 10 seconds after shock launch.

3.2 Mixing

In the following section, the differences in the formation and evolution of instabilities for the different explosion energies are studied. More particular, the 0.3B and 0.9B models are compared with each other, as well as with the one in which the piston driven explosion was triggered with energies of 0.6 B discussed by Chen et al. [2] to study dissimilarities.

3.2.1 0.6 B Model

To qualitatively compare the degree of mixing in the 0.3 and 0.9 models with the 0.6 B model of Chen et al.[2], an additional simulation with the same 0.6 B model energy is performed. Although the same stellar model and identical explosion energy and mechanism are used, the authors let the shock evolve for 20s in the 1D `KEPLER` stellar evolution code before mapping it onto the 2D `CASTRO` grid.

These ten seconds of offset between the two will have an impact on the evolution of the instabilities. Furthermore, the authors used the National Energy Research Scientific Computing Center (NERSC) located in Berkeley. During the implementation of the problem setup on the `Sciama` supercomputer a modification of the perturbation algorithm was necessary in order to guarantee a correct time step evolution. Figure 3.7 shows the evolution of mixing for our 0.6B model. The RT instabilities are now coarser than compared in the paper. Therefore these data is taken as the new baseline when comparing the evolution of instabilities and final yields.

Then again, the t=0s shot shows a difference as the present model displays the star 10s instead of 20s after the shock launch. This effect is reflected in a smaller radius of the high density central region. After 354s, the shock has travelled up to the helium and hydrogen shells of the star and already passed the inner layers. Here, formation of RT instabilities is clearly visible in the area corresponding to the intersection of carbon and

oxygen shells. They evolve most strongly at the inner boundaries but are also noticeable to start building up at the outer boundary. Additional instabilities are observable closer to the center, forming at the silicon shell. After almost 1200s, the instabilities evolved and continued mixing the material inside the star. Compared to the explosion in [2], the RT fingers at the outer boundary of the carbon shell do not show the same fine structure. After 2300s, the material in the central part of the star is strongly mixed while the process in the envelope of the star is much weaker than in comparison with [2].

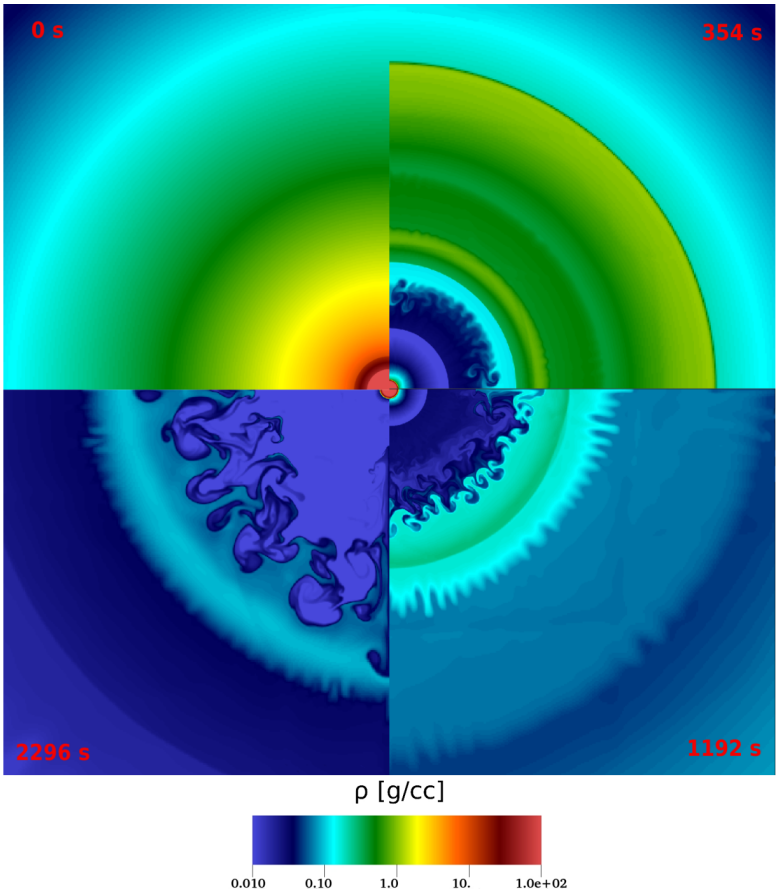

Figure 3.7: Star with 12.4 $M_\odot$ and explosion energy of 0.6B. Same model as in Chen et al. [2] but implemented on the `CASTRO` grid 10 seconds earlier. Panel sizes are $2 \cdot 10^{11}$ cm, respectively.

3.2.2 0.3 B Model

Already after 350s, differences in the evolution compared to the 0.6B model can be observed. As the 0.3B shock is weaker, resulting in a lower velocity of the material, the front has not propagated as far as the 0.6B equivalent.

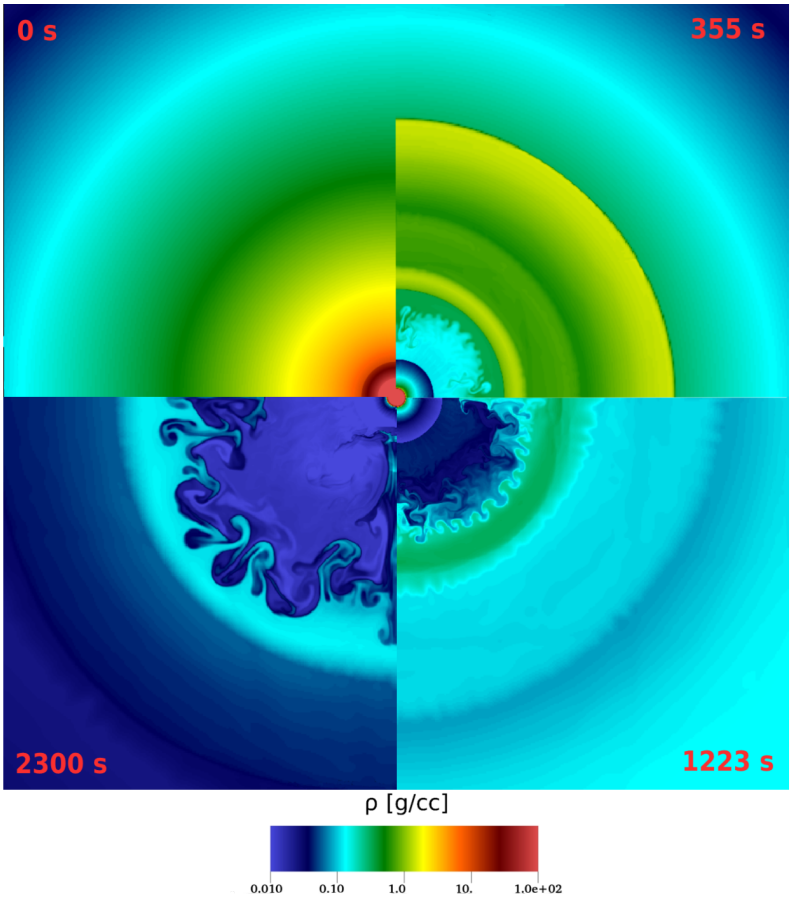

Figure 3.8: Star with 12.4 $M_{\odot}$ and explosion energy of 0.3B. Panel size is $2 \cdot 10^{11}$ cm on a side.

The first RT fingers are again forming at the inner boundaries of the oxygen and carbon shell. After 1200s, the backward shock has significantly mixed the inner shells. Instabilities are less prominent at the helium and hydrogen boarder, as well as at the oxygen helium shell than in the 0.6B model. This trend continues towards longer timescales. After 2300s, the mixing occurs to have evolved very similar to the 0.6B one.

However, the outer layers, that have already witnessed the shock breaking out of the star, show no notable mixing in the present simulation.

The formed fluid instabilities will continue their growth and expansion within the ejected material. While the backward shock propagates in the opposite direction, it drives mixing in the deeper layers until it eventually reaches the remnant in the center.

The outer layers of the progenitor have already expanded beyond the size of the computational domain. Material initially located in the deeper layers is heavily mixed as seen in figure 3.9.

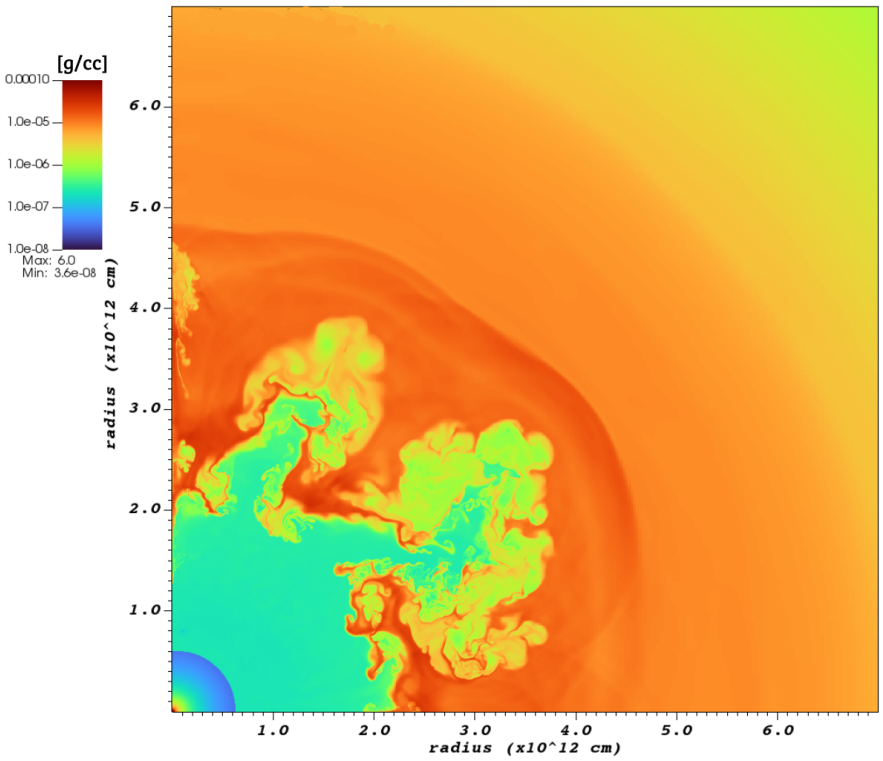

Figure 3.9: Fluid instabilities in 0.3B model $\sim$ 44000s after explosion. Panel size is $7 \cdot 10^{12}$ cm on a side.

Looking at the spatial distribution of some metals reveals the extend of their

propagation. Figure 3.10 shows the case for carbon, oxygen, neon and silicon. As seen from the blue circle in the center, indicating the initial radius of the star, their ejecta reached a distance measuring roughly five times the progenitors size. Inner layers of carbon, oxygen and neon are strongly mixed, while outer region show less mingling. Although the overall silicon layer displays a low degree of mixing, a significant fraction of the element is ejected from the supernova.

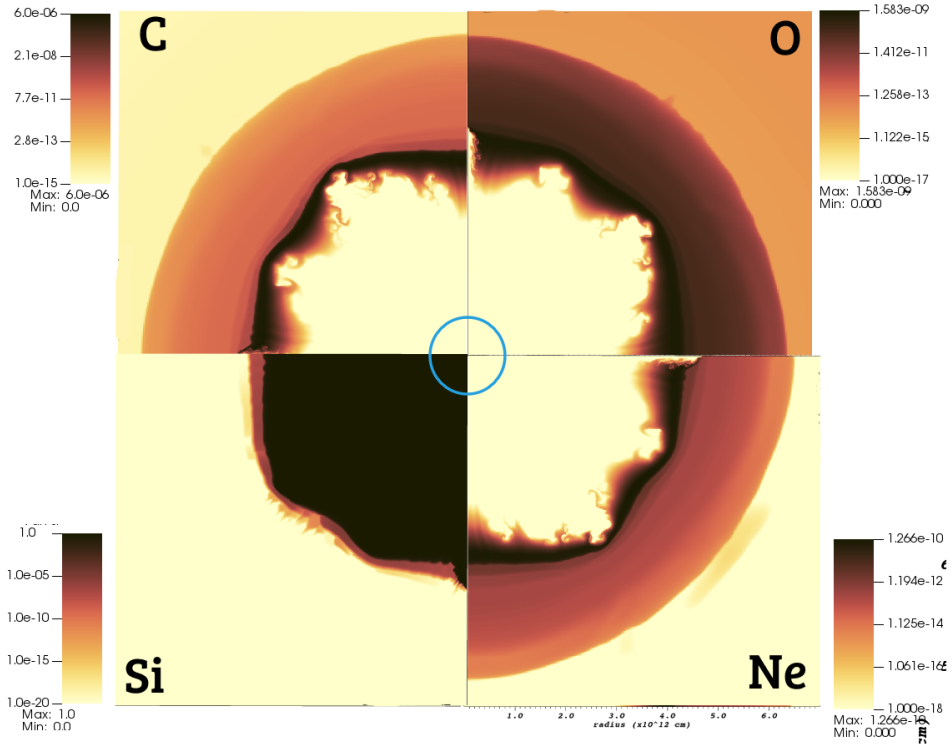

Figure 3.10: Spatial distribution of carbon, oxygen, neon and silicon in the 0.3B model $\sim$ 44000s after explosion. Blue circle indicates the size of the progenitor star. Panels are $7 \cdot 10^{12}$ on a side.

After fallback is essentially completed, the ejecta continue to expand homologously and enrich the interstellar medium as visualized in figure 3.11. To suppress the formation of a reverse shock that could drive additional mixing after shock breakout, a density profile of $\rho \sim r^{-3.1}$ for the circumstellar medium was chosen [2].

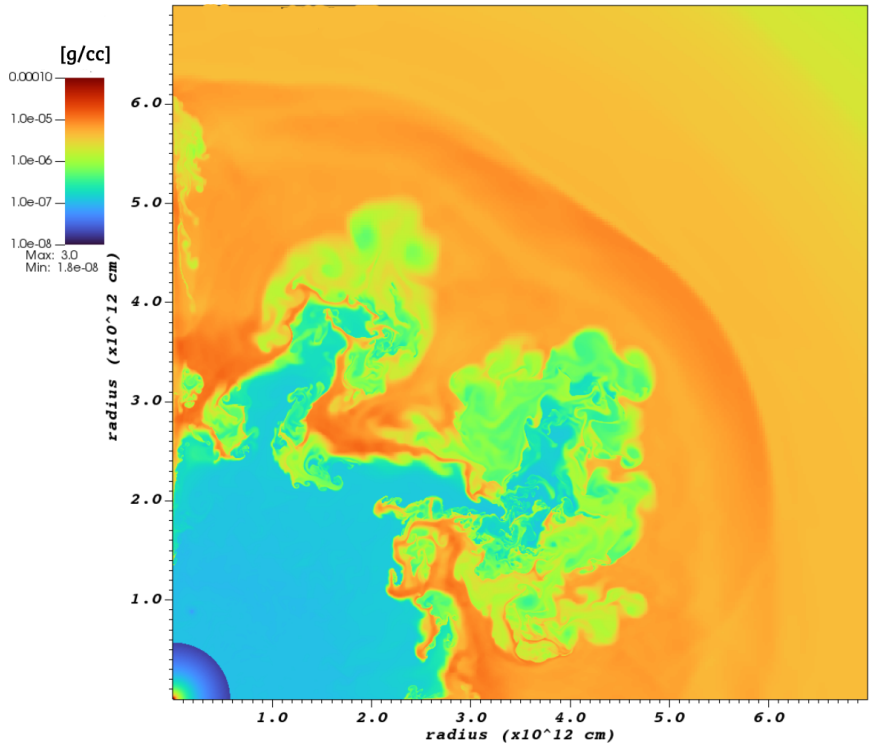

Figure 3.11: Homologous expansion of 0.3B model ejecta after 56000s. Panels are $7 \cdot 10^{12}$ on a side.

3.2.3 0.9 B Model

Joggerst et al. [25] studied, among others, mixing in core collapse supernovae for zero metallicity stars and three different explosion energies. Their progenitors were more massive and also the energies were higher, ranging from 0.6B to 2.4B. Their models show

stronger mixing for higher explosion energies, particularly for the inner layers of the star. Comparison of the 0.9B model to 0.6. and 0.3 shows a significantly higher degree of mixing in the outer layer of the carbon oxygen shell after 340s. Evolving the explosion until 1200s shows also a much stronger formation of instabilities. The size of the RT fingers formed at the inner boundary of the helium shell is more prominent than in the 0.6B equivalent. After 2300s, instabilities are clearly stronger within the outer structures of the model.

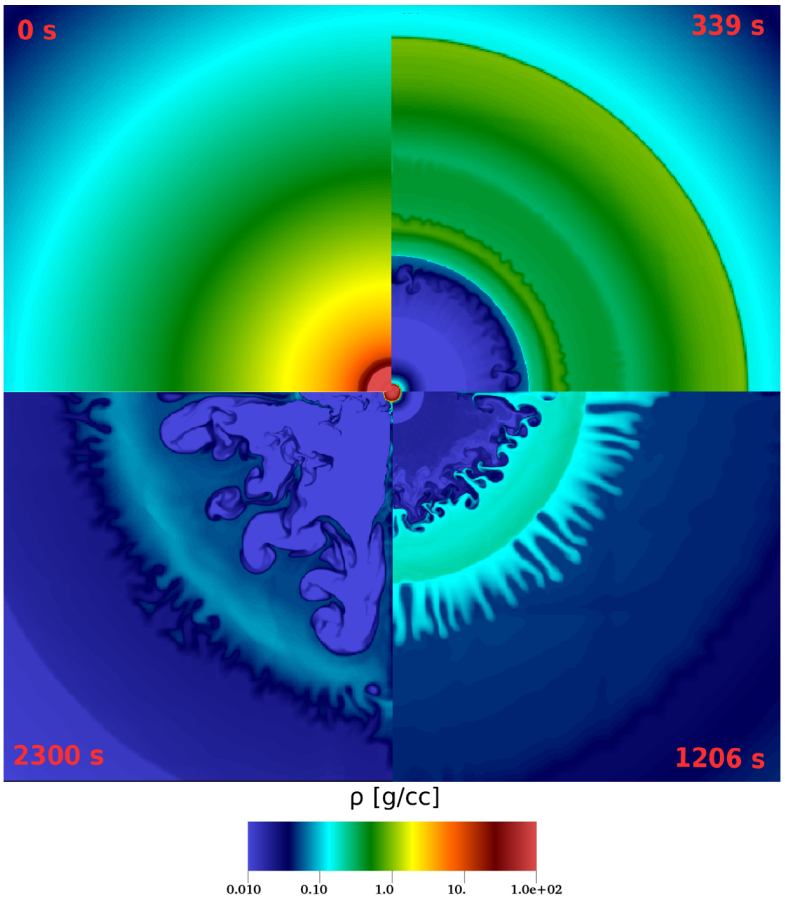

Figure 3.12: Star with 12.4 $M_{\odot}$ and explosion energy of 0.9B. Panel size is $2 \cdot 10^{11}$ cm on a side.

Mixing initiated by the reverse shock is completed by ~40000s in the 0.9B model. As seen in figure 3.13, the ejecta are mixed significantly stronger than in the previous 0.3B

model. Furthermore, the structure of the instabilities at the inner layer of the ejecta is much finer. Material in the outer layers on the other hand did not experience mixing of similar degree.

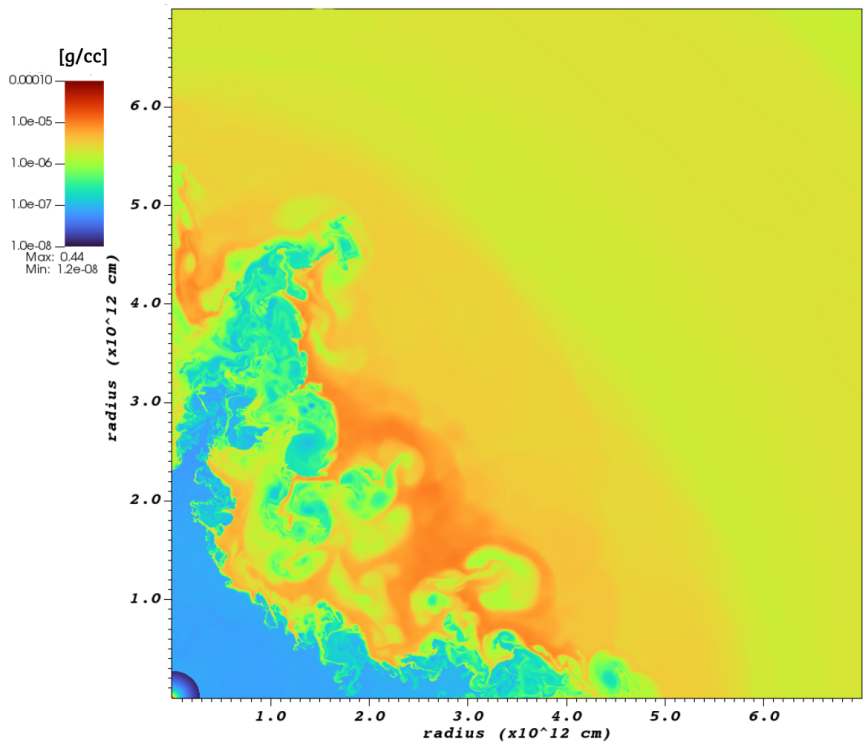

Figure 3.13: Fluid instabilities in 0.9B model $\sim$ 40000s after explosion. Panel size is $7 \cdot 10^{12}$ *cm* on a side.

Analysis of heavier elements confirms the more pronounced mixing in this explosion. Likewise, spatial distribution of carbon, oxygen, neon and silicon ejecta is studied as displayed in figure 3.13. All elemental layers display stronger mingling than observed in the 0.3B counterpart. Inner regions of the carbon, oxygen and neon show distinct structures of instability fingers that reach deeper into the outward directed material. Moreover, their abundances in the outer regions of the ejecta are higher, meaning that

the stronger explosion shock in addition spread these ejecta further outward. Silicon layers also show a higher dilation than in the 0.3B model.

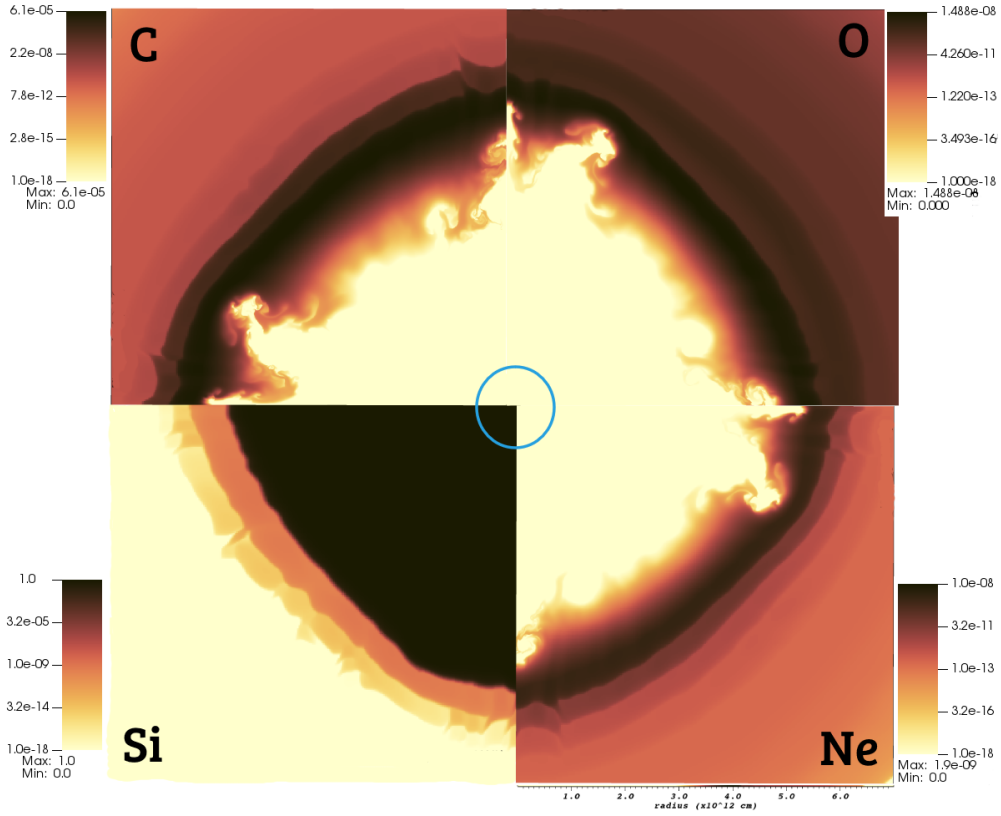

Figure 3.14: Spatial distribution of carbon, oxygen, neon and silicon $\sim$ in the 0.9B model 40000s after explosion. Blue circle indicates the size of the progenitor. Panels are $2 \cdot 10^{12}$ *cm* on a side.

After a total of 61500 s, the heavier metals ejected material moved way beyond five times initial progenitor's radius. Figure 3.15 displays the fluid instabilities at t = 61500 s. Escaped from the pull of the compact remnant, the ejecta will continue their homologous expansion and enrich the interstellar medium along its way.

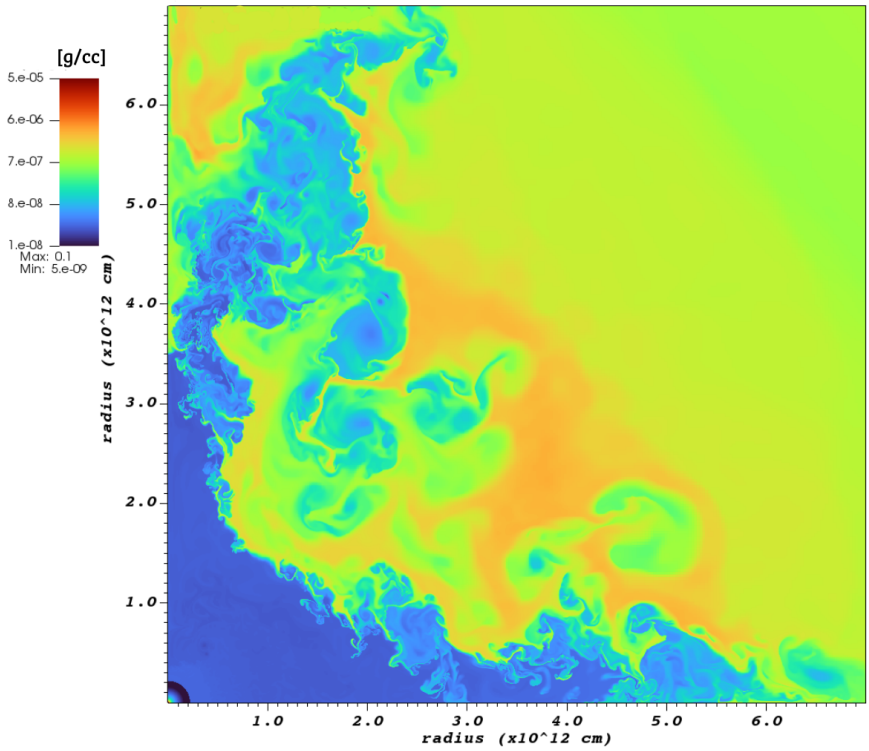

Figure 3.15: Homologous expansion of heavier element ejecta of 0.9B model. Panels are $7 \cdot 10^{12}$ on a side.

3.3 Fallback

While the shock propagates through the star and mixes the layers, some material will fall back onto the neutron star and thus not contribute to the final yields of the explosion. As the gravitational pull of the remnant defines an escape velocity, the degree of fallback is likely to increase towards lower explosion energies. The reverse shock plays a crucial role as well as it decelerates material which will then be accreted onto the neutron star. To study fallback in the 0.3B and 0.9B model, the direction of the fluid flows in both stars 200s after shock breakout is visualized. The shock breaks out of the surface from

the 0.3B model after 1995s in the 0.9B model after 1280s.

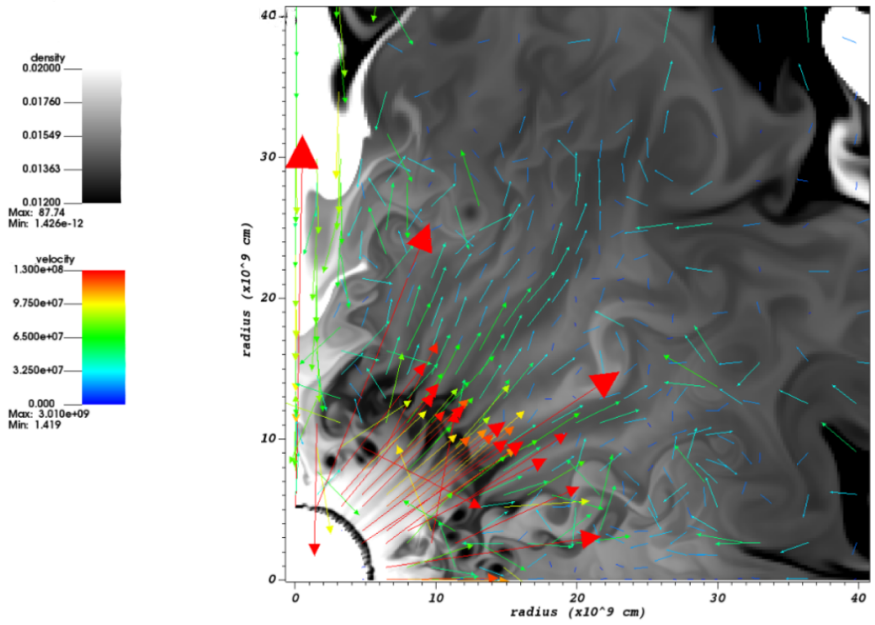

Figure 3.16: Fallback inside star with explosion energy of 0.9B at 1480s. The shock broke out of the surface 200s earlier, namely at 1280s after shock launch.

3.16 shows the inner region of the star 200s after the shock broke out of the star. The region is strongly mixed and there is clearly a significant amount of material that is accelerated towards the surface of the star. However, turbulent accretion flows are visible at some locations in the vicinity of the remnant. Strong fallback is indicated around the z pole region, although this process could be enhanced in the area because of pole effects induced by the numerical site of the simulation.
As the mass of the remnant grows continuously while fallback proceeds, making sure to wait long enough with the computation of the final yields in order to not overestimate the abundances of the ejecta is essential.

While the 0.9B model still shows active fallback 200s after the shock breakout, velocities of the material in the 0.3B model at the equivalent time step are much weaker. The flows

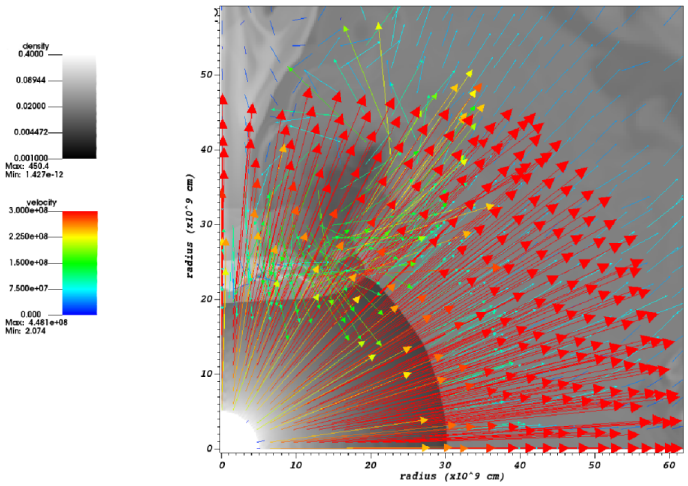

(a) Fallback in 0.3 B model at shock breakout

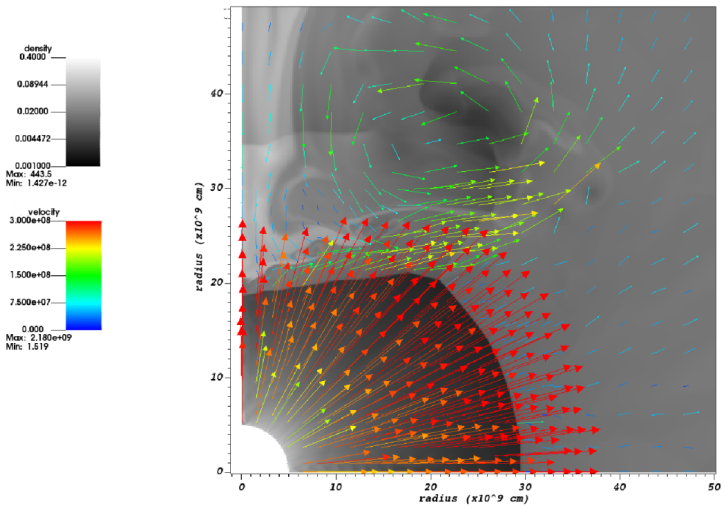

(b) Fallback in 0.3 B model 200s after shock breakout

Figure 3.17: Fallback inside the 0.3B model at the time of shock breakout at 1995s (top) and ≈200s after the shock plowed through the surface, namely 2175s

as displayed in 3.17b show that the motion of the material is mainly directed outwards. A prominent turbulence mixes the region in the upper part of the figure, creating fallback flows around the pole region of the star. For comparison, the snapshot 3.17a of the center at 1995s, the time when the shock breaks out of the surface reveals a stronger degree of fallback. Even though a considerable amount of material is moving outward, the region above the core shows strong turbulences which result in pronounced fallback motion. Likewise, to ensure the complete ceasing of fallback for a determination of final yields, the explosion needs to evolve on a longer timescale. The analysis of the turbulent motion around the center hints that the process should be finished even faster than expected for the low explosion energy compared to the 0.9B or even the 0.6B models.

3.4 Nucleosynthetic Yields

The nucleosynthetic yields are listed in tables 3.1 for the 0.3B model, table 3.2 for the 0.9B model.
Calculated by applying a mass cut deduced from equation 1.5 it excludes material and therefore elements having lower velocities. Lacking dredge up effects induced by mixing, yields deducted with this approach are therefore underestimating abundances of heavier isotopes, meaning $Z \geq 20$ [2].

Abundance ratios of J031300 were taken from [16]. These values for a total of 22 species were derived in their study from the MIKE/Magellan spectra. Thus, they comprise observed values and limits. Treated as maximum values, they are setting an upper limit on the abundances of the star.
Figure 3.18 shows a comparison between them and yields from the one dimensional `KEPLER` models. More precisely, abundances of ${}^{12}_{6}C$, ${}^{14}_{7}N$, ${}^{16}_{8}O$, ${}^{24}_{12}Mg$, ${}^{28}_{14}Si$, ${}^{32}_{16}S$, ${}^{36}_{18}Ar$, ${}^{40}_{20}Ca$, ${}^{44}_{22}Ti$, ${}^{48}_{24}Cr$, ${}^{54}_{26}Fe$ and ${}^{56}_{28}Ni$ are analysed.
Carbon, oxygen and magnesium ratios are in good agreement with the observed data.

Yields [$M_\odot$]	1D
^{1}H	6.47
^{4}He	3.99
^{12}C	0.11
^{14}N	$2.9 \cdot 10^{-9}$
^{16}O	0.23
^{20}Ne	$2.84 \cdot 10^{-2}$
^{24}Mg	$1.54 \cdot 10^{-2}$
^{28}Si	$3.76 \cdot 10^{-2}$
^{32}S	$1.22 \cdot 10^{-2}$
^{36}Ar	$1.95 \cdot 10^{-3}$
^{40}Ca	$1.33 \cdot 10^{-3}$
^{44}Ti	$6.44 \cdot 10^{-7}$
^{48}Cr	$2.99 \cdot 10^{-6}$
^{54}Fe	$2.55 \cdot 10^{-5}$
^{56}Ni	$4.23 \cdot 10^{-4}$
Ejected material	10.8
Neutron star	$1.6(1.47 + 0.13)$

Table 3.1: 1D yields of the 0.3B model.

Yields [$M_\odot$]	1D
^{1}H	6.47
^{4}He	3.99
^{12}C	$1.04 \cdot 10^{-1}$
^{14}N	$1.01 \cdot 10^{-8}$
^{16}O	0.2
^{20}Ne	$1.86 \cdot 10^{-2}$
^{24}Mg	$1.51 \cdot 10^{-2}$
^{28}Si	$5.7 \cdot 10^{-2}$
^{32}S	$2.4 \cdot 10^{-2}$
^{36}Ar	$4.7 \cdot 10^{-3}$
^{40}Ca	$4.07 \cdot 10^{-3}$
^{44}Ti	$2.85 \cdot 10^{-5}$
^{48}Cr	$6.54 \cdot 10^{-5}$
^{54}Fe	$6.89 \cdot 10^{-4}$
^{56}Ni	$6.9 \cdot 10^{-2}$
Ejected material	10.92
Neutron star	$1.48(1.47 + 0.01)$

Table 3.2: 1D yields of the 0.9B model.

Neither of both models is however able to reach the dimension of nitrogen abundance. Going towards higher atomic numbers, the discrepancies between 1D yields and J031300 abundances become even stronger. Titan, chromium and iron abundances are severely underestimated. By introducing a mass cut to define material that will fall back onto the remnant, isotopes below this specific radius are excluded and will not be present in the final yields. The mixing process that dredges up material located deeper in the ejecta is inadequately embraced in these calculations. Overall, comparing both one dimensional yields to J031300 abundances, the 0.3B model is in slightly better agreement than the 0.9B model. While the 0.9B explosion strongly overestimates silicon and calcium abundances, the 0.3B model's calcium yield is much closer to the observed value. Nickel yields are strongly overestimated for the 0.9B model, while the 0.3B model underestimates this quantity.

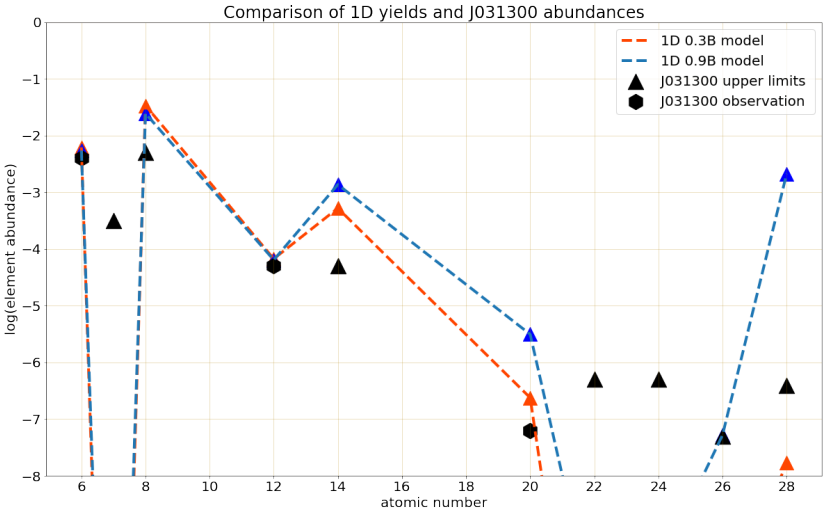

Figure 3.18: Comparison between 1D yields and abundances in J031300. Shown are yields for the 0.3B and 0.9B models as well as abundances of the metal poor star. Clearly, abundances for atomic number higher than 20 are heavily underestimated.

4 Discussion

Hydrodynamic simulations have been performed to model fallback and mixing in core-collapse supernovae. More precisely, the evolution of Rayleigh Taylor instabilities has been studied and the impact on the final nucleosynthetic yields.

While the calculated yields from the 1D models were in good agreement with abundances in J031300 for lighter metals, that is not the case for heavier ones, especially those with atomic numbers beyond 20. Due to the application of a mass cut in the process, they are strongly underestimated. Solely the nickel abundance in the 0.9B is an exception as it is overestimated. Regarding the mixing behaviour in the explosion models, this trend will most probably be enhanced by mixing. Through the resulting dredge up of material from the deeper layers, nucleosynthetic yields are expected to increase. For the 0.9B model in this case, it would lead to even higher silicon, calcium and nickel abundances which will be too high to match those of J031300.

For the 0.3B model however, an increase in the yields of heavier elements would have the potential to make it a suitable candidate for explaining the abundance pattern of J031300.

Overall, fluid instabilities are more pronounced in the 0.9 model than in the 0.3B model. Moreover, they start forming at earlier times. The stronger explosion shock causes the ejecta to expand more rapidly and additionally results in a stronger enrichment of the ejecta with metals.

Comparing the degree of mixing in the simulated explosions and the one in [2], significant

differences can be seen. For once because the algorithm computing and implementing the velocity perturbations on the model has been altered. Instabilities will nevertheless occur in locations that fulfill the necessary conditions. However, their growth is not further enhanced being probably responsible for the overall weaker evolution observed in the explosions. Further studies to analyse the impact of various perturbation algorithms on the mixing behaviour would be necessary for confirmation.

Another major difference is the time at which the models have been mapped onto the `CASTRO` grid after the shock launch. As the explosive nucleosynthetic burning should be finished after 10 seconds, we do not expect the abundances to be affected. Yet the impact of the shock travelling through the inner layers of the star in terms of instability formation may be affected as the propagation evolved 10 seconds longer on the one dimensional `CASTRO` grid. Joggerst et al. [12] discussed the possible impact of the mapping time between the grids on the mixing briefly as they observed a fewer amount of mixing in their zero metallicity models. More detailed studies about this factor need to be studied to asses the weight of the effect.

The underlying process leading to the explosion of the star as a supernova in the present studies was artificially induced by a piston, in other words the deposition of linear momentum near the center of the star. The implemented explosion mechanism will most likely have an impact not only on the isotopes and abundances generated during nucleosynthetic burning but also on the development of instabilities. Therefore studying the impact of the implemented explosion mechanism on mixing and fallback in supernovae modelling is crucial. Another approach similar to the piston induced technique is the thermal bomb method. There, the explosion is triggered by the deposition of internal energy, usually at the mantel of the pre-supernova model [32]. Other colleagues performed simulations modelling neutrino driven explosion models [33]. The collapse of the star into a neutron star releases a significant amount of energy in form of neutrinos. The binding energy that converted and release in the core collapse process is estimated being up to

more than 100 times higher than the supernova's kinetic energy and therefore considered as critical factor powering the supernova explosion.

As pointed out in [2], multidimensional simulations are the key to unravel realistic nucleosynthetic yields of supernovae explosions as fallback and mixing cannot be modelled in 1D. Especially the abundances of heavier elements with atomic numbers higher than 20 are significantly underestimated. While simulations in two dimensions are a big advancement in this field, even more realistic modelling in three dimension is indispensable. Joggerst et al. [34] performed three dimensional simulations in `CASTRO` and compared the growth of instabilities to the behaviour of the two dimensional case. Implementing the same proceeding as present in this thesis, they studied models with masses of $15 M_{\odot}$ but three different metallicities. In 3D models, the RT instabilities were observed to grow faster than in the 2D equivalents, matching with results by other colleagues [35]. However, they also tend to cease much faster, resulting in an overall identical mixed region width like in 2D.

Another point to investigate is the geometrical aspect of the explosion. For the simulations in this thesis, a spherical shape of both, the stellar progenitor and shock propagation were presumed. Observations of supernovae and particularly their remnants, for instance SN 1987a [36] or chemical asymmetries in Cassiopeia A [37] hint towards an asymmetrical behaviour of the process. Especially convective flows in connection with neutrino driven explosion mechanism in the very early stages following core collapse are considered to seed asymmetries. Studies of Janka et al. [38] studied this effect more in detail, concluding it could be responsible for expelling a higher amount of iron group elements through enhancing dredge up processes.

Due to their high masses and stability criteria, rotational velocities are presumed to be low for the very first stars. In the present simulations no rotational behaviour was applied. Joggerst et al. [25] studied in their simulations zero metallicity models with and without rotation. Latter die as compact blue supergiants while rotating counterparts

end their lives as red giants. Rotation induces additional mixing affecting mainly the structure of the stellar envelope while having little effect on the final nucleosynthetic yields.

Summarizing, huge improvements have been achieved in this field over the last two decades. Continuous improvement of computational capabilities boosted multidimensional supernova modelling, thus proceeding to improve our understanding of their explosion mechanism as well as evolution. Detailed studies analysing the degree of impact of parameters, like mechanism, perturbation algorithms, rotation an asymmetries etc. are inevitable in order to fully decode this phenomenon. Although the upcoming generation of telescopes will not observe PopIII stars directly, they will collect crucial data about their violent deaths as well as their successors. By combining these information, together with precise predictions of nucleosynthetic yields obtained in simulations, will continue to unravel the properties of the very first generation of stars. These findings will not only contribute in answering long lasting astronomical questions about the origin of quasars, seeds of supermassive black holes etc. but also about the chemical enrichment in the early universe, ultimately enabling us to pin down the earliest possible date of our universe in which the first habitable worlds may have been able to form.

Bibliography

[1] Hank Childs, Eric Brugger, Brad Whitlock, Jeremy Meredith, Sean Ahern, David Pugmire, Kathleen Biagas, Mark Miller, Cyrus Harrison, Gunther H. Weber, Hari Krishnan, Thomas Fogal, Allen Sanderson, Christoph Garth, E. Wes Bethel, David Camp, Oliver Rübel, Marc Durant, Jean M. Favre, and Paul Navrátil. Visit: An end-user tool for visualizing and analyzing very large data. In *High Performance Visualization–Enabling Extreme-Scale Scientific Insight*, pages 357–372. October 2012.

[2] Ke-Jung Chen, Alexander Heger, Daniel J. Whalen, Takashi J. Moriya, Volker Bromm, and Stan Woosley. Mixing of low energy population iii supernovae and the origin of extremely metal-poor stars. *MNRAS*, 467(4):4731–4738, June 2017.

[3] NASA. The story of our universe, 2021. Accessed Jul 09, 2022. `https://www.nasa.gov/mission_pages/planck/multimedia/pia16876b.html#.Ysm2VoRBwuU`.

[4] Michael Richmond. Star formation: the jeans criterion. Accessed Sep 25, 2022. `http://spiff.rit.edu/classes/phys370/lectures/starform/starform.html`.

[5] Volker Bromm. Formation of the first stars. *Reports on Progress in Physics*, 76(11):112901, oct 2013.

[6] Ralf Klessen. Formation of the first stars. In *Formation of the First Black Holes*, pages 67–97. World Scientific, apr 2019.

[7] Marco Loreggia, Anna Sancassani, Giulia Zuin. The virial theorem and its astronomical applications. Accessed Sep 25, 2022. `https://www.haus-der-astronomie.de/3440721/08Presentation_Virial_theorem.pdfl`.

[8] Daniel Whalen. Primordial universe. *Lecture Notes*, page 112901, SS19 2019.

[9] Naoki Yoshida, Kazuyuki Omukai, Lars Hernquist, and Tom Abel. Formation of primordial stars in a ΛCDM universe. *The Astrophysical Journal*, 652(1):6–25, nov 2006.

[10] Alexander Heger, S. E. Woosley, C. L. Fryer, and Norbert Langer. Massive star evolution through the ages. In *ESO Astrophysics Symposia*, pages 3–12. Springer-Verlag.

[11] Stirling A. Colgate and Richard H. White. The hydrodynamic behavior of supernovae explosions. *Astrophysical Journal*, 143:626, mar 1966.

[12] C. C. Joggerst, S. E. Woosley, and Alexander Heger. Mixing in Zero- and Solar-Metallicity Supernovae. *The Astrophysical Journal*, 693(2):1780–1802, mar 2009.

[13] Anton Vikaeus, Daniel J. Whalen, and Erik Zackrisson. Finding lensed direct-collapse black holes and supermassive primordial stars. *The Astrophysical Journal Letters*, 933(1):L8, jun 2022.

[14] Lucille H. Frey, Wesley Even, Daniel J. Whalen, Chris L. Fryer, Aimee L. Hungerford, Christopher J. Fontes, and James Colgan. The Los Alamos Supernova Light-Curve Project: Computational Methods. *The Astrophysical Journal Supplement Series*, 204(2):16, jan 2013.

[15] A. Heger and S. E. Woosley. The nucleosynthetic signature of population III. *The Astrophysical Journal*, 567(1):532–543, mar 2002.

[16] S. C. Keller, M. S. Bessell, A. Frebel, A. R. Casey, M. Asplund, H. R. Jacobson, K. Lind, J. E. Norris, D. Yong, A. Heger, Z. Magic, G. S. Da Costa, B. P. Schmidt, and P. Tisserand. A single low-energy, iron-poor supernova as the source of metals in the star SMSS j031300.36-670839.3. *Nature*, 506(7489):463–466, feb 2014.

[17] Anna Frebel and John E. Norris. Metal-poor stars and the chemical enrichment of the universe. In *Planets, Stars and Stellar Systems*, pages 55–114. Springer Netherlands, 2013.

[18] T.A. Weaver, G.B.Zimmerman, and S.E. Woosley. Presupernova evolution of massive stars. *The Astrophysical Journal Supplement Series*, 225:1021–1029, nov 1978.

[19] Ke-Jung Chen, Alexander Heger, and Ann Almgren. Conservative initial mapping for multidimensional simulations of stellar explosions. *Journal of Physics: Conference Series*, 402:012024, Dec 2012.

[20] Dr. Luca Grassitelli. Stars and stellar evolution computer lab. Accessed Sep 30, 2022. `https://astro.uni-bonn.de/~luca/lecture.pdf`.

[21] Castro Development Team. Castro: an adaptive mesh compressible hydrodynamics code. Accessed Jul 17, 2022. `https://amrex-astro.github.io/Castro/docs/index.html`.

[22] A. S. Almgren, V. E. Beckner, J. B. Bell, M. S. Day, L. H. Howell, C. C. Joggerst, M. J. Lijewski, A. Nonaka, M. Singer, and M. Zingale. CASTRO: A New Compressible Astrophysical Solver. i. Hydrodynamics and Self-Gravity. *The Astrophysical Journal*, 715(2):1221–1238, may 2010.

[23] Cornelis P. Dullemond. Equations of hydrodynamics. Accessed Sep 30, 2022. `https://www.ita.uni-heidelberg.de/~dullemond/lectures/num_fluid_2011/Chapter_1.pdf`.

[24] F. X. Timmes and F. Douglas Swesty. The accuracy, consistency, and speed of an electron-positron equation of state based on table interpolation of the helmholtz free energy. *The Astrophysical Journal Supplement Series*, 126(2):501–516, feb 2000.

[25] C. C. Joggerst, A. Almgren, J. Bell, Alexander Heger, Daniel Whalen, and S. E. Woosley. The Nucelosynthetic Imprint of 15–40 Solar Mass Primordial Supernovae on Metal-Poor Stars. *The Astrophysical Journal*, 709(1):11–26, dec 2009.

[26] IdealSimulations. Courant number. Accessed Sep 30, 2022. `https://www.idealsimulations.com/resources/courant-number-cfd/`.

[27] CASTRO development team. Timestepping and retrie - simulation time. Accessed Sep 30, 2022. `https://amrex-astro.github.io/Castro/docs/timestepping.html`.

[28] M. J. Turk, B. D. Smith, J. S. Oishi, S. Skory, S. W. Skillman, T. Abel, and M. L. Norman. yt: A Multi-code Analysis Toolkit for Astrophysical Simulation Data. *The Astrophysical Journal Supplement Series*, 192:9, January 2011.

[29] Charles R. Harris, K. Jarrod Millman, Stéfan J. van der Walt, Ralf Gommers, Pauli Virtanen, David Cournapeau, Eric Wieser, Julian Taylor, Sebastian Berg, Nathaniel J. Smith, Robert Kern, Matti Picus, Stephan Hoyer, Marten H. van Kerkwijk, Matthew Brett, Allan Haldane, Jaime Fernández del Río, Mark Wiebe, Pearu Peterson, Pierre Gérard-Marchant, Kevin Sheppard, Tyler Reddy, Warren Weckesser, Hameer Abbasi, Christoph Gohlke, and Travis E. Oliphant. Array programming with NumPy. *Nature*, 585(7825):357–362, September 2020.

[30] J. D. Hunter. Matplotlib: A 2d graphics environment. *Computing in Science & Engineering*, 9(3):90–95, 2007.

[31] University of Portsmouth. SCIAMA Supercomputer, note = Accessed Sep 29, 2022. `https://www.port.ac.uk/about-us/our-facilities/lab-and-testing-facilities/sciama-supercomputer`.

[32] Marco Limongi and Alessandro Chieffi. Evolution, explosion, and nucleosynthesis of core-collapse supernovae. *The Astrophysical Journal*, 592(1):404–433, jul 2003.

[33] Hans-Thomas Janka. *Neutrino-Driven Explosions*, pages 1–56. Springer International Publishing, Cham, 2017.

[34] C. C. Joggerst, A. Almgren, and S. E. Woosley. Three-Dimensional Simulations of Rayleigh-Taylor Mixing in Core-Collapse Supernovae. *The Astrophysical Journal*, 723(1):353–363, oct 2010.

[35] N. J. Hammer, H.-Th. Janka, and E. Müller. Three-Dimensional Simulations of Mixing Instabilities in Supernova Explosions. *The Astrophysical Journal*, 714(2):1371–1385, apr 2010.

[36] B. Sinnott, D. L. Welch, A. Rest, P. G. Sutherland, and M. Bergmann. Asymmetry in the outburst of SN 1987a Detected Using Light Echo Spectroscopy. *The Astrophysical Journal*, 767(1):45, mar 2013.

[37] B. W. Grefenstette, F. A. Harrison, S. E. Boggs, S. P. Reynolds, C. L. Fryer, K. K. Madsen, D. R. Wik, A. Zoglauer, C. I. Ellinger, D. M. Alexander, H. An, D. Barret, F. E. Christensen, W. W. Craig, K. Forster, P. Giommi, C. J. Hailey, A. Hornstrup, V. M. Kaspi, T. Kitaguchi, J. E. Koglin, P. H. Mao, H. Miyasaka, K. Mori, M. Perri, M. J. Pivovaroff, S. Puccetti, V. Rana, D. Stern, N. J. Westergaard, and W. W. Zhang. Asymmetries in core-collapse supernovae from maps of radioactive 44ti in cassiopeia a. *Nature*, 506(7488):339–342, feb 2014.

[38] Hans-Thomas Janka. Explosion mechanisms of core-collapse supernovae. *Annual Review of Nuclear and Particle Science*, 62(1):407–451, 2012.